27 Applications of Scanning Electrochemical Microscopy (SECM)

Gunther Wittstock · Malte Burchardt · Sascha E. Pust

Abbreviations and Symbols

c	concentration (moles per volume of solution)
c^*	concentration in bulk solution
d	working distance, distance between the active area of the UME and the sample surface
D	diffusion coefficient
dsDNA	double-stranded desoxy ribonucleic acid
ECSFM	electrochemical scanning force microscope
ECSTM	electrochemical scanning tunneling microscope
$E^{\circ\prime}$	formal potential of a redox couple
E_S	sample potential applied in SECM
E_T	potential applied at the SECM probe
F	Faraday constant
$F(L, \Lambda)$	$= (11/\Lambda + 7.3)/(110 - 40L)$
Fc	shortcut for a ferrocene derivative
Fc^+	shortcut for a ferrocinium derivative
GC	generation-collection mode of SECM
GDH	glucose dehydrogenase
GOx	glucose oxidase
Γ_{enz}	Surface concentration of an immobilized enzyme
HOR	hydrogen-oxidation reaction
i_S	electrolytic sample current or its equivalent in case of an enzyme reaction
I_S	normalized sample current $= i_S/i_{T,\infty}$
ISE	ion-selective electrodes
i_T	electrolytic current at the SECM probe
I_T	normalized electrolytic current at the SECM probe = $i_T/i_{T,\infty}$
I_T^{cond}	normalized electrolytic current at the SECM probe if the reaction at the sample is diffusion-controlled
I_T^{ins}	normalized electrolytic current at the SECM probe if there is no reaction at the sample
$I_{T,k}$	normalized electrolytic current at the SECM probe if a first-order reaction proceeds at the sample with a finite rate constant
$i_{T,\infty}$	electrolytic current at the SECM probe far from any surface
k_{cat}	catalytic turnover number
k_{eff}	first-order heterogeneous rate constant of the reaction at the sample

K_M	Michaelis–Menten constant
κ	dimensionless normalized first-order heterogeneous rate constant at the sample $= k_{eff} r_T / D$
L	normalized working distance $= d/r_T$
Λ	$= \kappa L = k_{eff} d / D$
n	number of transferred electrons per converted molecule
ORR	oxygen-reduction reaction
PAP	*p*-aminophenol
PAPG	*p*-aminophenyl-β-D-galactopyranoside
PQQ	pyrroloquinoline quinone
r_S	radius of the active region on a sample
r_T	radius of the active electrode area of a SECM probe
r_g	radius of the total probe diameter (radius of glass sheath)
RG	ratio between total probe radius and active electrode area $= r_g / r_T$
SECM	scanning electrochemical microscopy/microscope
SFM	scanning force microscopy/microscope
SG/TC	substrate generation/tip collection mode
ssDNA	single-stranded desoxy ribonucleic acid
STM	scanning tunneling microscopy/microscope
TG/SC	tip-generation/substrate collection mode

27.1 Introduction

27.1.1 Overview

Scanning electrochemical microscopy (SECM) is a technique that allows us to record spatially resolved maps of chemical reactivities, i.e. images that reflect the *rate of heterogeneous chemical reactions*. As with other scanning probe techniques, the acronym is used for both, the method and the instrument. SECM works in electrolyte solution and can be used to study reactions at insulating, semiconducting and conducting samples. The technique has found application in biotechnology (study of immobilized enzymes, development of biochips), cell biology (cell–cell communication processes), physiology (mass transport through biological tissue), corrosion science, and fuel-cell development. The SECM setup can be used to generate electrochemically precursor agents for surface modification. The combination of local surface modification and subsequent imaging of changes in chemical reactivities opens up new possibilities for the design of functional materials. Finally, the technique had and still has an enormous methodical impact on fundamental electrochemistry because the signal–distance curves (approach curves) contain a wealth of kinetic information. Besides the investigation of solid/liquid interfaces, it can also be applied to liquid/liquid and liquid/gas interfaces, where completely new insights have been obtained [1–5].

SECM instruments are commercially available and the number of groups using this technique is rapidly increasing. However, it can be noted that until now most

successful groups are rooted in fundamental electrochemistry and the application potential in other fields such as cell biology and material science has not yet been fully explored. This chapter aims at providing an overview of some important applications that reach beyond the scope of fundamental electrochemistry. The experiments will be explained qualitatively and, where it seems justified, quantitative treatment will be provided with a minimum of mathematical artwork. Some directions and requirements for future developments will be discussed as a summary and outlook that are closely interconnected with the Chapt. 8 in this volume by Kranz et al. For a systematic overview on the electrochemical principles and a comprehensive coverage of the theory the reader is referred to the authoritative book edited by Bard and Mirkin [1].

27.1.2 Relation to Other Methods

SECM is historically rooted in two experimental areas. As a scanning probe technique it shares many similarities with related techniques such as scanning force microscopy in an electrochemical cell (ECSFM) or electrochemical scanning tunneling microscopy (ECSTM). However, the signal in SECM is based on an electrochemical signal specific for a certain chemical compound dissolved in an electrolyte solution. In this respect the SECM probe can also be regarded as a positionable chemical microsensor. Two different microsensors can be used: amperometric electrodes and potentiometric electrodes. An amperometric electrode operates at an electrochemical potential (vs. a reference electrode). The measured Faradaic current results from the electrolysis of a compound contained in the solution. In most cases, the current is proportional to the concentration of the dissolved compound. Potentiometric probes have been used much less frequently (vide infra). They measure the equilibrium potential difference (i.e. at zero current) between an ion-selective electrode and a reference electrode. The potential difference is proportional to the *logarithm* of the activity (i.e. the effective concentration) of the potential-determining ion. Already in the early 1980s amperometric ultramicroelectrodes (UME) gained popularity among electrochemists because of the new opportunities offered by micrometer-sized electrodes for studying fast electrochemical reactions or for the detection of substances in restricted space [6], such as the detection of neurotransmitters in living organisms [7]. SECM has found broad application in the electrochemical community. This is not surprising, because a quantitative understanding of electrochemical reactions of various substances at microelectrodes had been already accumulated in the context of chemical sensing.

Looking back at almost two decades of SECM development, it seems logical to use an UME in order to measure the concentration distribution of reactants and products close to a macroscopic specimen (sample) electrode. The first experiment with scanning electrochemical microscopy was performed by Engstrom et al. [8]. At about the same time the group of Bard reported experiments with an electrochemical scanning tunneling microscope (ECSTM) where currents were observed at unusually large sample–tip distances. The signals were considered to be Faradaic currents, i.e. currents that result from the electrolysis of a chemical species at the metal tip. Bard and coworkers [9] realized that such a tip current can be influenced

by the presence of the sample in various ways. By 1989 Bard et al. had worked out an experiment in an analogous micrometer-sized system where all the effects could clearly be ascribed to well-understood physical processes such as diffusion or heterogeneous electrochemical reactions. With such an instrument quantitative agreement between the experimentally measured Faradaic currents and digital simulations was demonstrated for a few model systems [10, 11]. The simulation can provide quantitative results because the mass transport between the ultramicroelectrode and the sample under investigation is usually controlled by diffusion only, a theoretically well-understood phenomenon that can be described by continuum models with sufficient accuracy under the prevailing experimental conditions. Very soon it became evident that SECM is not just suitable to measure local solute concentrations but also, and more importantly, represents a tool to map local (electro)chemical reactivities, to induce localized electrochemical surface modifications, or to investigate heterogeneous and homogeneous kinetics. While lateral resolution in routine SECM experiments does not reach the resolution easily achieved with scanning force microscopy (SFM) or scanning tunneling microscopy (STM), the importance of SECM derives from its unique ability to analyze local fluxes of electroactive species. A brief introduction to SECM appeared in an earlier volume of this series [12].

27.1.3 Instrument and Basic Concepts

The general experimental setup is shown in Fig. 27.1. The local probe is an amperometric microdisk electrode (e.g. Pt) that is embedded in an insulating sheath, typically made from glass. Typical microelectrodes have electroactive probe di-

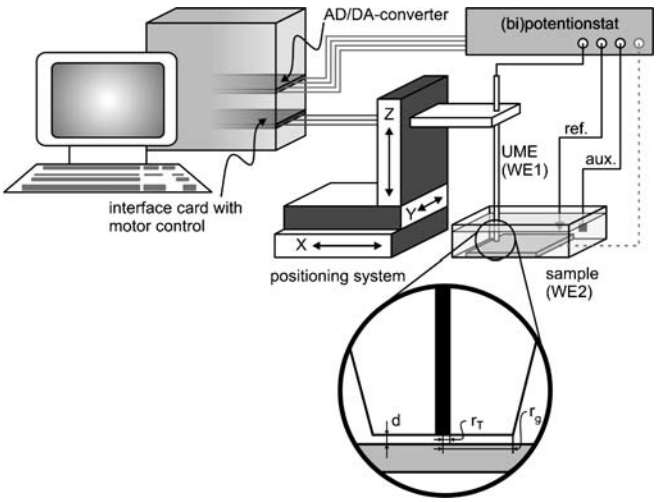

Fig. 27.1. Schematic setup of the SECM. Depending on the experiment, the sample may or may not be connected to the second channel of a bipotentiostat

ameters of 10 or 25 μm. Of course, electrodes with smaller diameters may be used and concepts of using nanoelectrodes are currently extensively explored. Prospects and limitations are discussed in Sect. 27.4. It is convenient to characterize the probe by two important radii: The radius r_T of the active electrode area and the radius r_g of the insulating glass sheath leading to the so-called RG value $RG = r_g/r_T$. The potential of the UME relative to a thermodynamically defined reference electrode is controlled by a (bi)potentiostat. For the investigation of enzymes and biological samples the specimen is usually not connected to an external voltage source. The probe is scanned in a distance d of (0.5–3) r_T across the sample. Various positioning systems have been used. It is important that the instrument allows a vertical movement of at least $20\,r_T$ in order to record useful approach curves.

27.1.3.1 Generation-Collection Mode

The generation-collection (GC) mode can be performed with amperometric and potentiometric probes. Usually, the detected compound is initially not present in solution and therefore, the concentration far from the surface approaches zero. The chemical microsensor (the collector) is used to detect dissolved chemical species that were generated or released from the sample (the generator). Specifically, this arrangement (mode) is called the substrate-generation/tip-collection mode (SG/TC) and is shown schematically in Fig. 27.2a. By detecting dissolved chemical species in the immediate vicinity of the specimen surface, this techniques lends itself to the characterization of surfaces at which substances are locally released into the solution or the study of localized mass transport, for instance through membranes.

Recently, the so-called tip-generation/substrate collection mode gained importance for combinatorial testing of electrocatalysts (see Sect. 27.3.2.2). In TG/SC mode the UME is used to produce a chemical species (e.g. O_2) from electrolysis of the solvent with a constant rate. The UME-generated O_2 diffuses to the sample region underneath the UME, where it is reduced at a finite rate (Fig. 27.2b). The reduction current at the sample is plotted versus the location of the UME and provides reaction-rate imaging for irreversible electrochemical reactions.

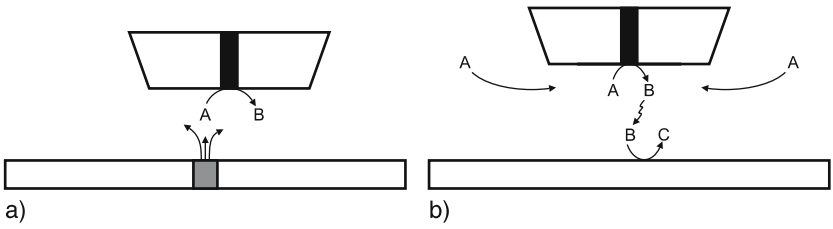

Fig. 27.2. Schematics of the GC mode. (**a**) Substrate-generation/tip-collection mode; (**b**) tip-generation-substrate-collection mode

27.1.3.2 Feedback Mode: Hindered Diffusion and Mediator Recycling

The feedback mode can be performed with amperometric probes only. Measurements are carried out in a solution containing an inert electrolyte (to provide ionic conductivity, typical 0.1–1 mol L^{-1}) and the oxidized or reduced form of a quasireversible redox couple ($R \rightleftharpoons O + ne^-$, e.g. (0.2–10) $\times 10^{-3}$ mol L^{-1}). R and O stand as generic symbols for a reduced compound (R, can be oxidized) and its corresponding oxidized compound (O, can be reduced). In close proximity of the UME to the sample, this compound shuttles electrons between the sample and the probe and is often called a "mediator". For further discussion it is assumed that initially only the reduced form R of the redox species is present.[1] The diffusion-limited current at an UME for the reaction $R \rightarrow O + ne^-$ in bulk solution is given by

$$i_{T,\infty} = 4nFDr_T c^* \,, \tag{27.1}$$

where n is the number of electrons transferred from each mediator molecule to the UME, F is the Faraday constant, D is the diffusion coefficient, r_T is the radius of the UME and c^* is the concentration of the mediator in bulk solution [13]. In analogy to other scanning probe techniques, the UME is frequently called "tip" from which the subscript "$_T$" was taken to specify quantities of the UME. Correspondingly, the subscript "$_S$" is used for quantities of the specimen (sample, substrate). The subscript "$_\infty$" indicates that the UME has a quasi-infinite distance to the surface. Practically $i_{T,\infty}$ is observed if the UME-sample distance d is larger than $20\,r_T$.

In order to ensure comparability, the current response in SECM is usually provided in dimensionless normalized units. The dimensionless UME current I_T is obtained by dividing the UME current i_T at a given position above the sample by $i_{T,\infty}$ ($I_T = i_T/i_{T,\infty}$). The dimensionless working distance L is the working distance d in units of r_T ($L = d/r_T$). If the UME approaches an inert and insulating surface, the diffusional flux of the electroactive species from the bulk solution to the active electrode area is hindered by the insulating glass sheath and the presence of the sample. The current, which is experimentally observed for inert insulating samples (e.g. glass) at an UME with $RG = 10$ is given by (27.2) [14] (Fig. 27.3, curves 1).

$$I_T^{ins}(L) = \frac{i_T}{i_{T,\infty}} = \frac{1}{0.40472 + \frac{1.60185}{L} + 0.58819\exp\left(\frac{-2.37294}{L}\right)} \,. \tag{27.2}$$

The oxidized form O can be rereduced ($O + ne^- \rightarrow R$) at the sample surface, if i) the sample is electronically conducting, ii) O is consumed in a catalytic reaction at the sample surface, or iii) the sample is etched by O. After a fraction of a second, a steady-state current will be established, at which the consumption of R at the UME is balanced by the diffusional resupply of R from the bulk phase of the solution and the diffusion of R regenerated by the reaction at the sample surface. Only sample regions located under the active area of the UME will significantly contribute to the regeneration process of the mediator [15]. Plotting changes of the current versus tip location provides the basis for imaging in SECM.

[1] Of course all experiments can be performed by initially providing only the oxidized form of the mediator. In this case all reactions are reversed.

If the reaction at the sample and at the UME are both diffusion-controlled, the maximum current for any given UME position and solution composition is obtained. This upper limit of the current response is given by (27.3) [14].

$$I_{\mathrm{T}}^{\mathrm{cond}} = \frac{i_{\mathrm{T}}}{i_{\mathrm{T},\infty}} = 0.72627 + \frac{0.76651}{L} + 0.26015 \exp\left(\frac{-1.41332}{L}\right) . \qquad (27.3)$$

The curve is given in Fig. 27.3, curve 2. Experimental approach curves to samples with finite kinetics are located in-between the two limiting cases (Fig. 27.3, curves 3–6, for details see Sect. 27.2.1.2). This situation allows two basic experiments to be carried out: Scanning the UME at constant distance provides an image that reflects the distribution of heterogeneous reaction rates of the sample. Moving the UME vertically towards the sample, allows a more detailed kinetic investigation of the reaction $O + ne^- \rightarrow R$ at a specific location of the sample. Examples for both cases will be discussed in Sects. 27.2.1.1 and 27.2.1.2.

The communication and interdependence of the reactions at the sample and at the UME lead to the term "feedback mode" for this special mode within SECM [11, 16]. In the context of SECM the term "feedback" does *not* refer to an electronic circuit and actuator maintaining a constant probe-sample interaction as is common in other scanning probe microscopies.

When comparing the feedback mode and the GC mode, it has become evident that the GC mode is more sensitive to slow reaction rates and the feedback mode provides better lateral resolution. These guidelines will be illustrated and further substantiated within the following section.

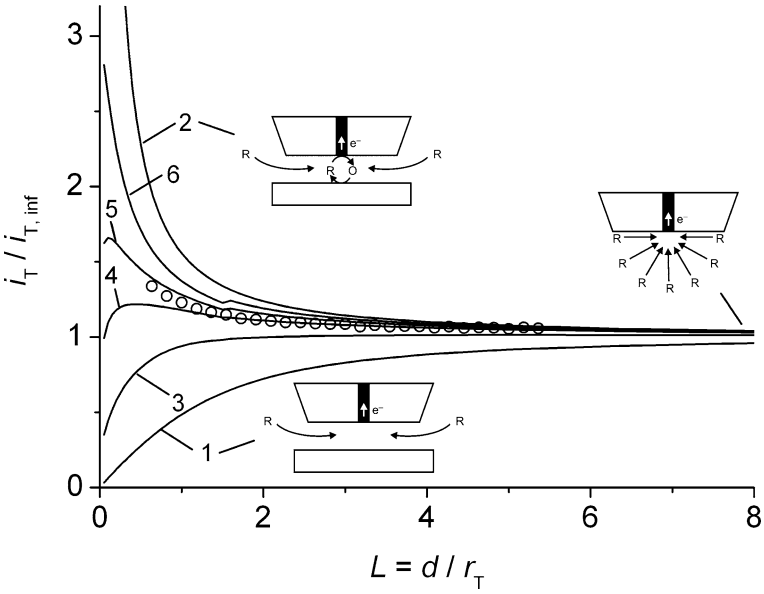

Fig. 27.3. SECM approach curve towards a GDH-modified modified surfaces (*open symbols*). For comparison calculated curves for hindered diffusion (*1*), diffusion-controlled reaction at the sample (*2*) and normalized rate constants $\kappa = k_{\mathrm{eff}} r_{\mathrm{T}} / D$ are given: 0.3 (*3*), 1.0 (*4*), 1.8 (*5*), 3.6 (*6*)

27.2 Application in Biotechnology and Cellular Biology

Since the inception of SECM, attempts have been made to apply the technique to investigations of biologically or biochemically relevant problems [17]. Measurements with the SECM are conveniently performed in buffered aqueous solutions, a preferred environment for most biological samples. The scanning electrode does not physically contact the specimen and therefore does not interfere with the sample compared to alternative scanning probe techniques, e.g., STM and SFM. The electrochemical detection of metabolites via SECM can be used to map biochemical activity thereby complementing techniques that image the topography of biological specimens or biomolecules. A systematic overview of SECM investigations at biological systems can be found in two authoritative review chapters [18, 19]. When sorting the various applications, grouping them according to the complexity of the investigated biological entity seems adequate and will be used in this chapter.

27.2.1 Investigation of Immobilized Enzymes

With respect to biological samples, isolated enzymes immobilized to a solid support were the first systems investigated with SECM. Enzymes can be divided into seven classes depending on the catalyzed reaction type. The largest group are oxidoreductases, i.e. enzymes that catalyze redox reactions. Such enzymes are technically relevant as biorecognition elements in biosensors, in enzyme-loaded columns or membranes for biotechnological conversions or in biofuel cells.

27.2.1.1 Characterization of Oxidoreductases in the SECM Feedback Mode

In order to illustrate the imaging principle, we consider the investigation of pyrroloquinoline quinone (PQQ)-dependent glucose dehydrogenase (GDH, EC 1.1.99.17) [20]. It is the classic example of PQQ-dependent quinoproteins, a large group of enzymes that can convert alcohols and amines to their corresponding aldehydes/lactones [21]. PQQ-dependent GDH catalyzes the transfer of 2 electrons and 2 protons from glucose to a soluble n-electron acceptor M_{ox} ($n = 1, 2$).

$$\text{D-glucose} + (3-n)M_{ox} \xrightarrow{[\text{GOx}]} \text{D-gluconolactone} + (3-n)M_{red} + 2\text{H}^+ \,. \tag{27.4}$$

The electron acceptors can serve as electron mediators between the active center of the enzyme and an electrode surface. GDH has a very high catalytic activity. For example, approximately 3 mmol of glucose is oxidized per minute per milligram of protein with 2,6-dichlorophenol indophenol, which is up to 20 times the activity of pure glucose oxidase (GOx) [22]. The high activity and independence of oxygen make GDH extremely interesting for developing biosensors and immunoassays technology [22, 23]. These applications require that the enzyme kinetics of the immobilized enzyme can be characterized. Furthermore, miniaturized sensors, which

are increasingly demanded for high throughput testing or multianalyte sensor arrays would benefit from spatially resolved measurements.

A model sample was prepared by binding GDH to streptavidin-coated magnetic microbeads [20]. The magnetic microbeads were arranged as a mound supported on a polymer foil via an external magnetic field [24]. The resulting mound is shown in Fig. 27.4a.

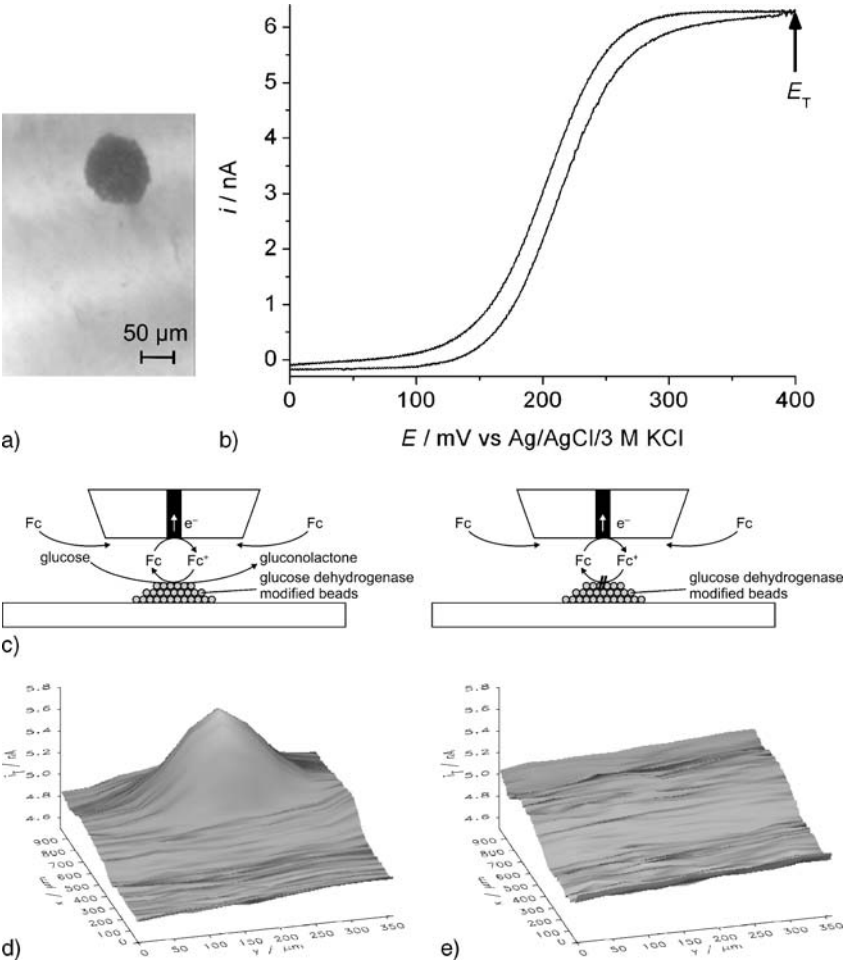

Fig. 27.4. SECM feedback imaging of GDH-modified microbeads. (**a**) optical photograph of the bead assembly. Individual beads have a diameter of 3 µm. They are not resolved in the optical image; (**b**) cyclic voltammogram for the oxidation of Fc to Fc^+ at the UME; (**c**) Schematic of the SECM experiment in the presence and absence of glucose; Fc, ferrocene methanol; (**d**) SECM feedback imaging in a solution containing 2 mM ferrocene methanol as mediator and 50 mM D-glucose in buffered solution. (**e**) Control experiment the same area as in (**d**) in a buffer solution containing 2 mM ferrocene methanol but *no* glucose. From [20] Copyright 2004, American Chemical Society

A set of experiments is performed in the presence and absence of the enzymatic substrate glucose. This approach is outlined in Fig. 27.4c. The buffered solution keeps the pH value close to the optimum pH value of the enzyme. In addition, it provides the ionic conductivity without being electrochemically converted at the electrode. Secondly, the solution contains a redox mediator, specifically ferrocene methanol (Fc) in Fig. 27.4. Ferrocenes are metal organic compounds in which a divalent iron ion is sandwiched between two cyclopentadienyl anions. Substitutions at the cyclopentadienyl rings allow the solubility, the overall charge and the redox potential of the compound, to be tuned. In this experiment ferrocene methanol was selected for the following reasons: i) It can be reversibly oxidized to the ferrocinium form (Fc^+) at the UME. The ferrocinium ion consists of a trivalent iron ion that is sandwiched between two cyclopentadienyl anions. Because of the absence of major structural changes during this redox reaction, the electrochemical reaction is fast and reversible. ii) Fc^+ is able to act as an electron acceptor (M_{ox} in (27.4)). iii) The solution contains glucose as a substrate for the enzyme. Glucose is not converted at the working potential E_T of the UME.

Table 27.1. SECM feedback imaging of local activity of immobilized oxidoreductases

Enzyme imaged	Substrate	Mediator/reaction at the UME	Ref.
Glucose oxidase, EC 1.1.3.4	50–100 mM glucose	0.05–2 mM ferrocene monocarboxylic acid, dimethylaminomethyl ferrocene (oxidation)	[24–26]
		0.05–2 mM $K_4[Fe(CN)_6]$ (oxidation)	[25]
		0.02–2 mM hydroquinone (oxidation)	[25, 27]
		0.5 mM [Os fpy $(bpy)_2$Cl]Cl, fpy = formylpyridine, bpy = bipyridine (oxidation)	[26]
PQQ-dependent glucose dehydrogenase, EC 1.1.99.17	50 mM glucose	0.05–2 mM ferrocene monocarboxylic acid 0.05–2 mM ferrocene methanol 0.05–2 mM *p*-aminophenol (oxidation)	[20]
NADH-cytochrome C reductase, EC 1.6.99.3 within mitochondria	50 mM NADH	0.5 mM N,N,N′,N′-tetramethyl-*p*-phenylenediamine (oxidation)	[27]
Diaphorase (NADH acceptor oxidoreductase, EC 1.6.99.-)	5.0 mM NADH	0.5 mM hydroxymethyl ferrocene (oxidation)	[28]
Horseradish peroxidase, EC 1.11.1.7	0.5 mM H_2O_2	1 mM hydroxymethyl ferrocenium (reduction)	[29]
Nitrate reductase, EC 1.7.99.4	23–65 mM NO_3^-	0.25 mM methylviologen (reduction)	[30, 31]

In order to perform an experiment, the UME is first positioned in the bulk solution and a cyclic voltammogram is recorded. In this experiment, a triangular potential profile is applied to the working electrode and the resulting current is recorded (Fig. 27.4b). If the UME potential E_T exceeds the formal potential $E^{\circ\prime}$ of the Fc/Fc^+ redox couple, a steady-state diffusion-limited current, $i_{T,\infty}$ is observed. The potential E_T of the UME for subsequent imaging is selected such that a diffusion-controlled current is observed.

When the UME is located above the sample regions with immobilized enzymes, Fc^+ formed at the UME reaches the enzyme and acts as an electron mediator enabling a conversion at the sample according to (27.4). Figure 27.4d shows an experimental image. The increased currents in the center are caused by the additional flux of the mediator when the UME is located above the enzyme-modified beads. A negative control experiment was performed by imaging the same area after exchanging the solution with a glucose-free buffered solution containing Fc. In this case the enzymatic reaction cannot proceed because the substrate glucose providing electrons to the enzyme is absent. The corresponding image in Fig. 27.4e shows a rather uniform current across the entire area. This current exclusively originates from the diffusional transport of Fc from the solution bulk to the active UME area.

The described principle has been applied to a number of enzymes within the oxidoreductase family that are important in the context of biosensors or biofuel cells (Table 27.1).

27.2.1.2 Quantification of Enzyme Kinetics Using the Feedback Mode

Soon after developing the initial SECM experiments, it was realized that this method could evolve into a new tool for the *quantitative* determination of the kinetics for a variety of interfacial reactions. The basic concept is outlined here under omission of exact deviations. Other reviews provide a broad coverage on this subject [1]. The diffusion-limited current according to (27.1) is the experimental current that is observed at sufficiently positive potentials, e.g. at $E_T = 400\,mV$ (Fig. 27.4b). The current at any given position of the UME above the sample is obtained from a partial differential equation (or a set of them). The kinetic behavior of the sample is entered as one of the boundary conditions. Such partial differential equations have been numerically solved for a variety of relative UME–sample positions (indexed k) and kinetic properties of the sample [15, 32]. Results of several simulations $I_{T,k} = f(L_k)$ for discrete working distances L_k have been interpolated by analytical functions $I_T = f(L)$ facilitating further analysis. Several proposed analytical functions are available in the literature [14, 33–35]. We restrict our discussion to one selected example in closest agreement with the presented experimental results [14]. In general, the differences between these functions do not exceed experimental uncertainties. The calculated function $I_T = f(L)$ is experimentally obtained by moving the UME slowly ($1\,\mu m\,s^{-1}$) from a large distance ($d > 10\,r_T$) towards the sample surface. Therefore, such experiments are commonly called approach curves, although the curve superimposes with the retract curve because a quasisteady-state situation is reached at each location. Such approach curves are the equivalent to force–distance curves in SFM and contain a wealth of kinetic information. The

experimental approach curves (Fig. 27.3, open symbol) towards a GDH-modified surface using ferrocene methanol as mediator is located in-between the two limiting cases (Fig. 27.3, curves 1 and 2). This is the typical situation for sample surfaces with limited heterogeneous kinetics.

The experimental approach curves can be described by

$$I_T(L) = \frac{i_T}{i_{T,\infty}} = I_T^{ins}(L) + I_S^{kin}(L)\left(1 - \frac{I_T^{ins}(L)}{I_T^{cond}(L)}\right) . \tag{27.5}$$

The normalized substrate current $I_S^{kin} = i_S/i_{T,\infty}$ is the current equivalent at the sample normalized by the UME current in bulk solution. It can be estimated considering the following three conditions: i) the distance range is $0.1 < L < 1.6$, ii) $RG \approx 10$ and iii) the reaction at the sample is of first order with respect to the mediator.

$$I_S^{kin}(L, k_{eff}) = \frac{0.78377}{L\left(1 + \frac{1}{\Lambda}\right)} + \frac{0.68 + 0.3315\exp\left(\frac{-1.0672}{L}\right)}{1 - F(L, \Lambda)} , \tag{27.6}$$

where $\Lambda = \kappa L$; $F(L, \Lambda) = (11/\Lambda + 7.3)/(110 - 40L)$, and $\kappa = k_{eff} r_T/D$ [33]. The curves for various κ values are also given in Fig. 27.3. From the agreement of the experimental curve and the calculated curve 4 in Fig. 27.3, one can conclude $\kappa = 0.55$ for this experiment. Using the experimentally determined diffusion coefficient of the mediator $D = 7.25 \times 10^{-6}\,cm^2\,s^{-1}$, and $r_T = 12.5\,\mu m$ (from an optical micrograph or from an experimental approach curve to glass and a fit to (27.2)), an effective first-order rate constant for the enzymatic reaction at the sample of $6 \times 10^{-3}\,cm\,s^{-1}$ is obtained.

The general form of the expression for an enzyme that transfers two electrons to a one-electron mediator [25] is given by

$$f_{Fc^+} = -f_{Fc} = \frac{k_{cat}\Gamma_{enz}}{\frac{K_{M,gluc}}{c_{gluc}} + \frac{K_M}{c_{Fc^+}} + 1} . \tag{27.7}$$

$K_{M,gluc}$ and K_M are the Michaelis–Menten constants of the enzyme with regard to glucose and Fc^+, respectively. Γ_{enz} is the surface concentration of the enzyme and k_{cat} is the catalytic turnover number of the enzyme. Using glucose concentrations $c_{gluc} \gg K_{M,gluc}$ and mediator concentrations $c^*_{Fc} \ll K_{M,Fc}$, one obtains a pseudofirst-order rate law with an effective rate constant given by

$$k_{eff} = \frac{k_{cat}\Gamma_{enz}}{K_M} . \tag{27.8}$$

Such approach curves have been obtained for several mediator concentrations. By subtraction of I_T^{ins} (27.2) from the experimentally obtained curve using (27.5), $I_{S,K}$ is obtained and can be used in order to verify the first-order nature of the reaction and to obtain a K_M value for various mediators [20]. If Γ_{enz} is known from an independent experiment, k_{cat} of the immobilized enzyme can be determined [20].

The analysis outlined can be applied in essence to a number of different reactions at samples that can be described by first-order heterogeneous kinetics, e.g. electrochemical reactions, ion and electron transfer at liquid/liquid interfaces, surface etching, etc. Hence, SECM is an extremely versatile technique for the investigation of interfacial reactivities.

27.2.1.3 Investigation of Immobilized Enzymes in the Generation-Collection Mode

Despite the possible quantification of the immobilized enzyme activity, it should be noted that feedback-mode analysis (and imaging) of enzymes has to deal with some principal limitations: The analysis is only valid if the enzyme is immobilized at an insulating support, e.g. a membrane. If the enzyme is immobilized at a conductive surface, e.g. an electrode of an amperometric biosensor, recycling of the mediator will in most cases be superseded by the electrochemical recycling of the mediator at the sample (electron transfer from the electron conductor to the mediator "bypassing" the enzyme) [26]. If the sample is not connected to an external voltage source, it will assume an electrochemical potential controlled by the concentration of the reduced and oxidized mediator in the solution. Since the oxidized form (in our example) is only present in the vicinity of the UME and everywhere else the reduced form is in large excess, the conducting sample will assume a potential that corresponds to the reduced mediator. Between the region directly under the UME (where the oxidized form prevails) and the sample regions further away, a *concentration cell* is formed that can drive the reduction of the mediator very efficiently even in the absence of an enzyme or an externally applied potential. Most oxidoreductases already work in the regime of zero-order kinetics at millimolar concentration levels of the mediator, which are convenient for SECM measurements. This substantially decreases the sensitivity of the analysis. Furthermore, only oxidoreductases can be investigated, other enzymes cannot be imaged. The generation-collection (GC) mode, specifically the sample-generation/tip-collection mode provides a viable alternative for all these limitations since it is more sensitive and the response is independent of the nature of the immobilization substrate (conductive or insulating).

The schematic for GC imaging of GDH is shown in Fig. 27.5a. In contrast to the feedback experiment in Fig. 27.4c, the electron acceptor for GDH ($[Fe(CN)_6]^{3-}$) is contained in the bulk of the working solution and the enzymatic reaction independently proceeds of the presence of the UME. A diffusion layer develops above the active regions of the sample and the local concentration is probed by the UME. A typical experimental example is shown in Fig. 27.6 for the enzyme galactosidase [36]. Galactosidase is an important marker enzyme and is also used as a label in various biotechnological applications and in im-

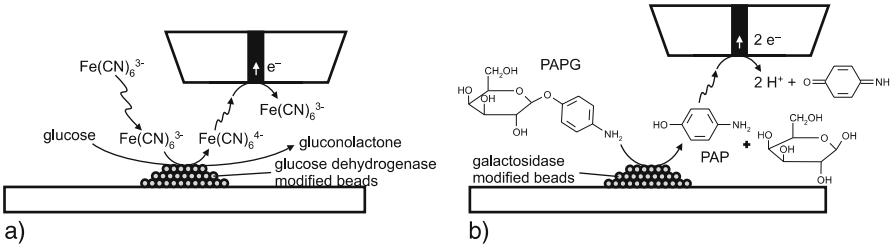

Fig. 27.5. Schematic for the GC mode for the enzyme (**a**) GDH and (**b**) galactosidase

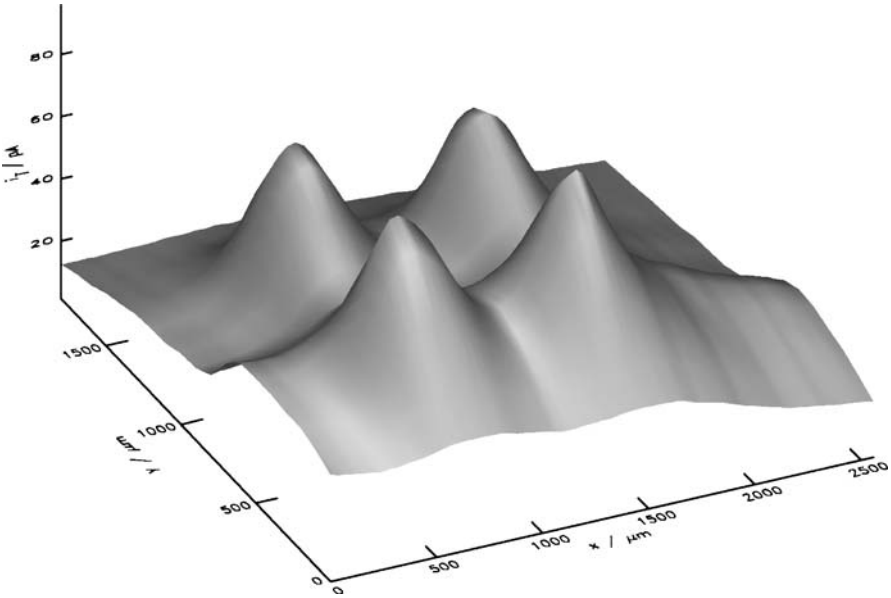

Fig. 27.6. GC-mode imaging of an array of surface-modified bead mounds labeled with galactosidase. Reprinted from J. Electroanal. Chem., 561, C. Zhao, J.K. Sinha, C.A. Wijayawardhana, G. Wittstock, Monitoring β-galactosidase activity by means of scanning electrochemical microscopy. 83–91, Copyright 2004, with permission from Elsevier Science

munoassays. In principle, this enzyme can not be imaged by the feedback mode, since it does not belong to the oxidoreductases. The "trick" to make its activity "visible" to SECM is based on the chosen substrate (*p*-aminophenyl-β-D-galactopyranoside, PAPG). Galactosidase catalyzes the formation of *p*-aminophenol (PAP) from PAPG (Fig. 27.5b). PAP can be oxidized at a lower potential than PAPG, which allows imaging of the diffusion layers formed above immobilized galactosidase. There is a wide variety of substrates available for photometric activity tests of enzymes that can be used directly or after appropriate chemical modifications.

Table 27.2 provides an overview of the enzymes that have successfully been imaged in GC mode. The following guidelines may be helpful for investigation of immobilized enzymes via a feedback experiment or a GC experiment. If the enzymes are immobilized at a conducting surface, the GC mode is more suitable. The achievable lateral resolution in GC mode is lower than in the feedback mode, however, it can be improved by coupling to further homogeneous or heterogeneous reactions [38]. The GC mode for investigating enzymes is significantly more sensitive than the feedback mode. It is less sensitive to topographic features and can operate at larger working distances, which is an advantage for corrugated samples. An experimental comparison of the two operation modes in the context of biosensor research is available in the literature [44]. The feedback mode allows a more precise quantification of the kinetics. The GC mode can also be used with ion-selective electrodes as probes, provided that there is a mecha-

Table 27.2. SECM imaging of local enzyme activities in the GC mode

Enzyme	Species detected at the UME	Probe	Ref.
Glucoseoxidase EC 1.1.3.4	H_2O_2	Amperom. Pt UME Amperom. enzyme electrode	[37, 38] [39]
PQQ-dependent glucose dehydrogenase, EC 1.1.99.17	$[Fe(CN)_6]^{4-}$	Amperom. Pt UME	[20]
urease EC 3.5.1.5	H^+ NH_4^+	Potentiom. Sb UME Liquid membrane ISE	[40] [41]
Horse radish peroxidase EC 1.11.1.7	Ferrocene derivatives	Amperom. Pt UME	[29, 42, 43]
Alkaline phosphatase EC 3.1.3.1	4-aminophenol	Amperom. Pt UME	[24, 44–47]
Galactosidase EC 3.2.1.23	4-aminophenol	Amperom. Pt UME	[36, 48]
Alcoholdehydrogenase EC 1.1.1.1	H^+	Potentiom. Sb UME	[49]
NADPH-dependent oxidase in osteoclasts	$O_2^{\bullet -}$	Cytochrome-c-modified Au UME (amperom.)	[50]

nism to vertically position the electrode. After all, it is not surprising that many more investigations related to practical applications have been performed in GC mode, whereas feedback mode dominates in fundamental studies. This observation extends beyond imaging of enzymes. However, a successful design of SECM experiments requires fundamental understanding of both mechanisms: A complete experiment usually includes both working modes, e.g. feedback experiments are used to position the UME at a defined distance from the sample using (27.2) and then a GC image is recorded. Secondly, GC contributions may disturb feedback experiments and feedback contributions can be present in GC experiments that either disturb a quantitative analysis, or which can be exploited for enhancing the sensitivity [48]. A substantial extension of the GC-mode applications can be expected if miniaturized biosensors are used as probes, as demonstrated by Kueng et al. [51, 52].

27.2.1.4 Quantification in the GC Mode

With some limitations, GC experiments can also be quantified. Most applications approximate the UME as a noninteracting probe, i.e. a probe that only senses the local concentration but does not affect the local environment by conversion of one species. While this is fulfilled for ISE, it is only an approximation for an amperometric microelectrode. The approximation is justified if the UME is considerably smaller than the active region at the sample, and if the working distance is larger than $3r_T$. It is advantageous if the RG value of the UME is small ($RG < 5$). In order to form a steady-state diffusion layer above the sample, the active regions at the sample must be microstructures and spaced with at a sufficiently large distance ensuring that the diffusion layers do not overlap. The analysis basically follows a simple

diffusion model that describes how a compound diffuses through a disk-shaped pore into an acceptor compartment [53, 54]. The current at the UME can then be calculated in analogy to (27.1) where the bulk concentration c^* is replaced by the local concentration at the position of the microelectrode. This local concentration $c = c_S\theta$ can be derived from the concentration at the pore opening c_S and a geometry-dependent, dimensionless dilution factor θ. They are related to i_T by

$$i_T = 4nFDr_T c_S\theta \ . \tag{27.9}$$

The factor θ depends on the lateral distance r and vertical distance d of the UME from the center of the active region. For a single horizontal scan (x) across the center of the spot, θ can be described as follows:

$$\theta = \frac{2}{\pi}\arctan\frac{\sqrt{2}r_S}{\sqrt{\left(\Delta x^2 + d^2 - r_S^2\right) + \sqrt{\left(\Delta x^2 + d^2 - r_S^2\right)^2 + 4d^2r_S^2}}} \ . \tag{27.10}$$

A fit of an experimental line scan to (27.9) and (27.10) provides c_S. An example of a line scan across a GDH-modified surface is given in Fig. 27.7. The current for the oxidation of $[Fe(CN)_6]^{4-}$ formed during the enzymatic reaction is plotted vs. location. The experimental current can be fitted to (27.9) and (27.10). The total flux Ω from the bead spot can be calculated by [13]

$$\Omega = 4Dc_S r_S \ . \tag{27.11}$$

From the total flux Ω, the area (πr_S^2) of the active region, the surface concentration of the enzyme Γ_{enz}, and the catalytic turnover number $k_{cat} = \Omega(\pi r_S^2)/\Gamma_{enz}$ can be

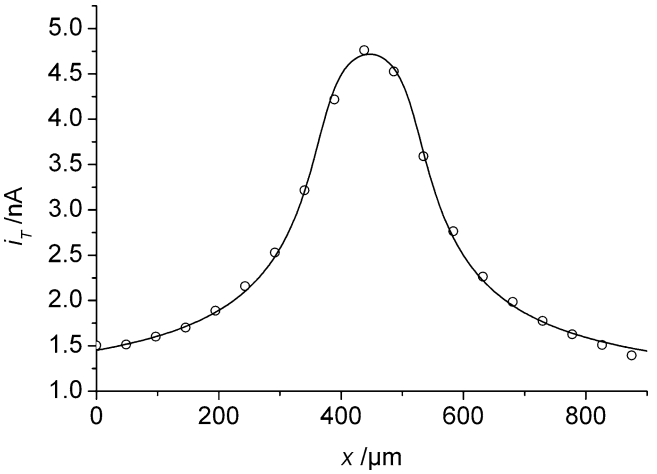

Fig. 27.7. Fitting of a GC line scan across a GDH-modified bead mound to (27.9) and (27.10). Experimental parameters $c^*_{[Fe(CN)_6]^{-3}} = 10$ mM, $d = 30$ µm, $r_S = 75$ µm. The *solid line* was calculated from (27.9) and (27.10) with the following parameters $c_{S,[Fe(CN)_6]^{-4}} = 1.69$ mM, $d = 30.45$ µm, $r_S = 74.35$ µm, $D_{[Fe(CN)_6]^{-3}} = 6.19 \times 10^{-6}$ cm^2 s^{-1}, and a constant current offset of 0.91 nA for all points. From [20] Copyright 2004, American Chemical Society

estimated for the immobilized enzyme, when the substrate concentrations are much higher than K_M (zero-order reaction) [20].

27.2.1.5 SECM for Read-Out and Optimization of Biochips and Biosensors

Microstructured biosensor surfaces have been investigated by SECM [17,55]. These investigations were mainly prompted by the idea to produce compartmentalized surfaces, where some regions are surface modified in order to provide an ideal environment for the biochemical component while other regions are optimized for electrochemical detection [56, 57]. Furthermore, SECM can be applied to locally modify surfaces [28, 43, 58–67] by different defined electrochemical techniques. The combination of the imaging capabilities for specific enzymatic reactions and the possibility of modifying the surfaces in a buffered solution make SECM an ideal tool to explore the potential of such micropatterned surfaces for sensing applications.

Another set of applications relies on the opportunity of recognizing many biochemicals by a specific antibody chemically linked to an enzyme label. Herein, SECM can be used to detect the enzyme label [47]. In this application, SECM can be an alternative to fluorescence detection. However, the main disadvantage of SECM in this respect can be seen in long experimental time, lack of high throughput and the required skills of the experimentator. On the other hand, the sensitivity of the detection is comparable, the required instrumentation is less expensive and common problems in optical detection such as background fluorescence are of no concern in SECM. Given these circumstances, electrochemical techniques will be important for protein arrays, where a limited number of analytes is detected. Due to its flexibility, SECM is ideally suited for the optimization of such protocols. A readout for a mass-produced assay can then be realized in microstructured electrochemical cells using the SECM working modes but avoiding the mechanically demanding and time-consuming scanning [68, 69].

Matsue et al. [29, 42, 70, 71] have developed a number of biochips based on the described principle. Among these biochips are multianalyte assays for human placental lactogen (HPL), human chorionic gonadotropin (HCG) [42] and leukocidin, a toxic protein produced by methicillin-resistant *Staphylococcus aureus* [71]. Figure 27.8 shows an example of a dual immunoassay with SECM detection. Different antibodies were immobilized at specific regions of the chip. After exposure to a solution containing HPL and HCG, the analytes were bound by the antibody. The chip was then exposed to a mixture of horesradish-peroxidase (HRP)-labeled antibodies against HPL and HCG. After adding the substrate for the enzymatic reaction H_2O_2 and ferrocene methanol (Fc), as the electron acceptor the readout is made by recording the current for the reduction of ferrocinium methanol (Fc^+) at the UME. Fc^+ is produced locally at the chip surface by the enzyme HRP under consumption of H_2O_2. In this way the analyte is defined by the position on the chip and the amount of analyte is quantified via the collection current at the UME.

Microbeads can be used as a new platform for immunoassays and a model assay for immunoglobulin G (IgG) has been demonstrated by Wijayawardhana et al. [45, 72] with alkaline phosphatase as the labeling enzyme. Detection limits down to 6.4×10^{-11} mol L^{-1} or 1.4×10^{-15} mol mouse IgG could be demonstrated.

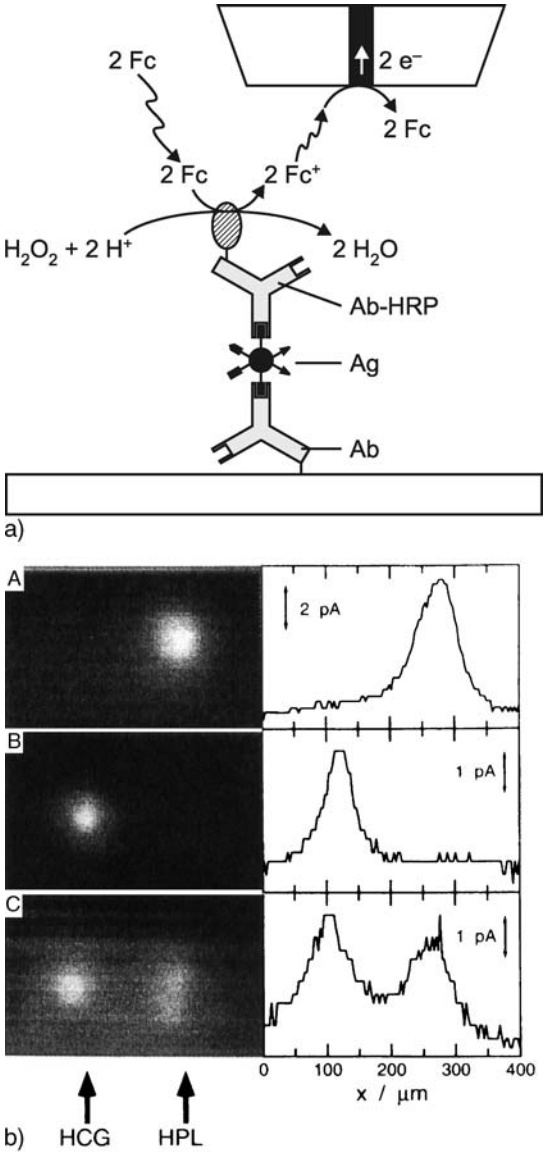

Fig. 27.8. (**a**) Scheme of the SECM detection in a sandwiched immunoassay. (**b**) SECM images and cross-sectional profiles of microstructured glass supports with (anti-HCG)-Ab and (anti-HPL)-Ab immobilized at two distinct regions, treated with **A** 56 ng mL^{-1} HPL; **B** 2.0 IU mL^{-1} HCG; **C** a mixture containing 31 ng mL^{-1} HPL + 0.63 IU mL^{-1} HCG. After rinsing, the glass support was dipped into a solution of 20 µg mL^{-1} (anti-HCG)-Ab-HRP + 7 µg mL^{-1} (anti-HPL)-Ab-HPL. Working solution: 1.0 mM Fc + 0.5 mM H_2O_2 + 0.1 M KCl + 0.1 M phosphate buffer, pH 7.0; $v_t = 9.8$ µm s^{-1}; $E_T = +0.05$ V (Ag/AgCl). Reprinted from J. Electroanal. Chem., 438, H. Shiku, Y. Hara, T. Matsue, I. Uchida, T. Yamauchi, Dual immunoassay of human chorionic gonadotropin and human placental lactogen at microfabricated substrate by scanning electrochemical microscopy. 187–190, Copyright 1997, with permission from Elsevier Science

Since the *p*-aminophenol produced by the enzyme-catalyzed reaction was detected close to the point of origin, an incubation step for enzymatic amplification could be avoided.

More recently, another application of SECM detection in DNA and protein chips and in electrophoresis gels has emerged with different detection principles. Wang et al. [73] labeled single-stranded DNA (ssDNA) with gold nanoparticles. After binding to their complementary strand at the chip surface, silver was electroless deposited at the metallic particles. The formed metal features were imaged in the

feedback mode with $[Ru(NH_3)_6]^{3+}$ as mediator, in which the mediator is regenerated by a electron transfer to silver metal at those regions of the sample surface, where a thin silver film was formed. A similar approach was used by Carano et al. [74]. Proteins were blotted on poly(vinylidene difluoride) membranes. The model protein bovine serum albumin was then tagged with previously prepared silver nanoparticles. The position of the protein bands was detected by SECM using $[Os(bpy)_3]^{2+}$ as a mediator, which was oxidized at the UME. The oxidized mediator diffused to the sample surface and induced the oxidation and dissolution of the deposited silver nanoparticles, which were not interconnected to each other. In these applications, the exact quantitative relation between the SECM signal and the amount of analyte is not well understood and it is empirically established by calibration curves that might be sensitive to a number of interfering factors that are difficult to control.

Wang and Zhou [75] detected hybridized DNA on a chip by electrogenerating $[Ru(bpy)_3]^{3+}$ at the UME in a SECM experiment. $[Ru(bpy)_3]^{3+}$ is a strong oxidation reagent and can oxidize the base guanine, present in DNA. Where DNA was located at the chip, the reaction between guanine and the oxidized form of the mediator resulted in an enhanced current at the UME.

Turcu et al. [76, 77] immobilized ssDNA at microspots at a gold surfaces. The location of the ssDNA could be imaged using the negatively charged redox mediator ($[Fe(CN)_6]^{3-/4-}$) in SECM feedback mode. The mediator regeneration proceeded by a heterogeneous electron transfer to the gold surface of the chip. At the spots of the negatively charged ssDNA, the diffusion of the negatively charged mediator to the gold surface was blocked and a reduced feedback current was observed. The observed current was further reduced, when hybridization with the complementary strand occurred and the negative charge at the surface was increased.

Fortin et al. [78] reported an alternative detection scheme based on an enzymatic amplification without imaging the enzyme activity in feedback mode. They produced the DNA microarray by depositing a polypyrrole pattern using a procedure developed earlier by Kranz et al. [79]. By using a mixture of pyrrole and functionalized monomers covalently attached to a 15mer ssDNA oligomer, polypyrrole spots were formed carrying the 15mer oligomer as single DNA strand [80]. Hybridization was performed with biotinylated complementary ssDNA strands. After reaction with streptavidin and biotinylated horseradish peroxidase, the enzymatically catalyzed oxidation of soluble 4-chloro-1-napthol to insoluble 4-chloro-1-naphton was used to create an insoluble, insulating film at the polypyrrole spots. SECM imaging with the mediator $[Ru(NH_3)_6]^{3+}$ visualized these regions by reduced currents compared to the bare gold surface [78].

27.2.2 Investigation of Metabolism of Tissues and Adherent Cells

Electroanalytical techniques such as the patch clamp technique, miniaturized ISE and surface-modified carbon microelectrodes for the detection of neurotransmitter release from nerve cells are routinely used in physiological studies, both at the cellular level and at the level of entire organs [7]. Therefore, it seems viable to use SECM to gain deeper insights into structure–function relationships important in biological research. This potential had been recognized very early in SECM

development and it essentially relies on the same principles that were outlined for the investigation of immobilized enzymes. However, some additional challenges emerge when working with cellular systems and current instrumental developments are aiming to overcome these obstacles. In conventional SECM imaging, the UME is scanned parallel to a flat surface in order to keep the working distance d constant. This approach is sufficient if the roughness of the sample is negligible compared to the (electro)active UME radius r_T, which is typically 5–20 μm. In contrast, cells represent corrugated objects with height differences in the micrometer range, i.e. similar or even larger in size compared to r_T. Hence, the UME has to follow the topology of the sample in order to keep a constant d similar to the approaches used in other scanning probe techniques such as STM. Derived from Fig. 27.3 it becomes evident that this task is more challenging in conventional SECM. The current–distance relationship may vary significantly depending on the chemical nature of the sample. Therefore a constant-current imaging is not feasible. The current may decrease upon approach of the probe (inert surface) or increase (reactive surface). Therefore, it is impossible to select a setpoint that would be appropriate for an entire sample. Furthermore, using a constant-current approach would limit the possibility to quantify the SECM response with respect to chemical reactivities. In order to overcome the difficulties in positioning the UME above corrugated objects, a number of approaches have been used. The microelectrode can be positioned with the help of an optical microscope at a fixed location with respect to the biological specimen and the release of a specific substance is followed after stimulation [50, 81, 82]. Alternatively, cells can be cultivated in specifically designed conical microcavities, forming a flat surface [65, 83–85]. The UME scans in a constant distance over the openings. Alternatively, dual-electrodes have been used for positioning [86]. One electrode records the redox current of a mediator conversion that does not interact with the sample. For this compound the current is controlled exclusively by (27.2) and is used as the distance-dependent signal. The second electrode of the dual electrode assembly detects the species of biological interest that is released from the biological entity. Several attempts exist to design a setup by means of feeding back a *current*-independent signal into an actuator that keeps d constant. The most convincing results could be obtained by systems that detect mechanical shear forces between an UME that vibrates parallel to the sample surface with amplitude in the nanometer range ($\ll r_T$). Since the electrodes are immersed in a viscous solution, stable detection of the shear forces appears to be challenging. The vibrations can be excited by a tuning fork similar to the concept in scanning near-field optical microscopy [87–90]. However, since the resonance frequency is determined by the tuning fork but the UME represents usually a higher mass than the legs of the tuning fork, the mechanical resonator tends to be ill-defined and the number of published examples is rather limited, despite the high expectations that have been raised earlier. Another approach excites the microelectrode with a frequency tuned to the mechanical properties of the microelectrode itself. The vibration amplitude is detected either by projecting a diffraction pattern produced by a light-emitting diode onto a split photodiode [91] or by detecting the vibration amplitude with a second piezo attached to the UME [92]. Both approaches have been largely popularized in the SECM community by the work of Schuhmann et al. [62, 93–98]. Meanwhile, a commercially self-standing shear force system is available that can be attached

to any well-designed SECM instrumentation. Nevertheless, the use of a shear-force system adds another level of complexity to the experiment because the mechanical properties of the UME, the sample and the entire setup become important and have to be optimized.

27.2.2.1 Imaging Photosynthetic Oxygen Production

SECM was used to map the topography and the rate of photosynthetic oxygen production of a leaf still attached to an intact plant, *Tradescantia fluminensis* [81]. The leaf was fixed at the base of the electrochemical cell. The entire setup was placed inside a glove bag to control of the environment (Fig. 27.9). Illumination of the leaf was achieved by shining light through an optical fiber attached to a xenon lamp from the base of the electrochemical cell. Since electrochemical redox mediators are often toxic to living organisms, oxygen was chosen to image the topography of the leaf in the dark (no O_2 production by the leaf) by exploiting (27.2) [23]. Although the electrochemical reduction of oxygen involves a more complicated scheme, it is

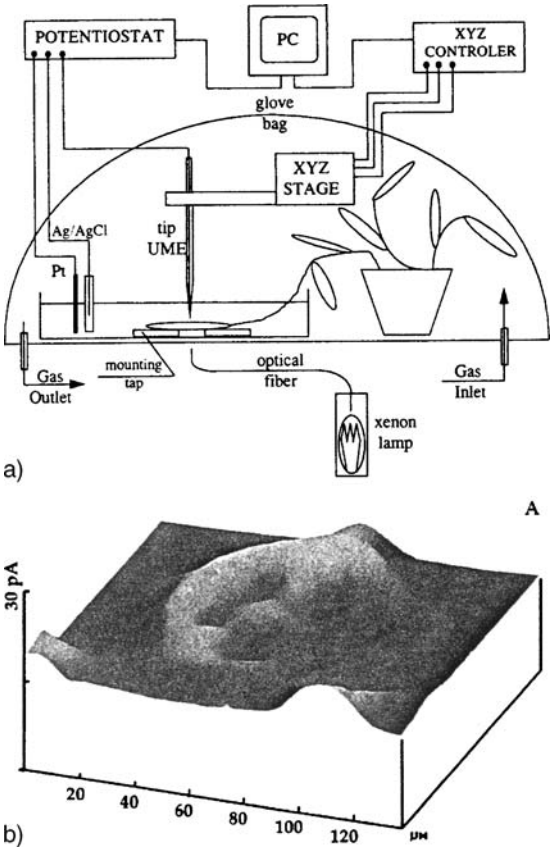

Fig. 27.9. (**a**) Experimental setup to study local oxygen production at leaf surfaces. (**b**) Oxygen release from a single stomatal complex in the white leaf region of *Tradescantia fluminensis*. (Reprinted with permission from [81] Copyright American Society of Plant Biologists)

a logical choice for studying living systems. It has to be assured that E_T is poised at a sufficiently negative value to ensure a current that is proportional to the bulk concentration of O_2 and the solution is buffered to compensate the pH shift induced by the proton transfer accompanying the O_2 reduction. Individual stomatal complexes were clearly resolved with the protruding guard cells appearing as depressions in the UME current image and the stomatal pore in the center of the complex as a current peak in agreement with (27.2) that predicts a decrease of i_T if d is reduced by protruding sample regions. *T. fluminensis* possesses white regions in which chloroplasts are only present in the guard cells around the stomata. The stomata were sufficiently widely separated that the oxygen diffusion layers did not overlap and hence, generation-collection mode imaging could be performed. The images recorded during illumination (O_2 production in the chloroplasts of the guard cells) showed a peak current roughly a factor of two higher than the O_2 background over the stomata. Tsionsky et al. [81] were able to image the photosynthetic oxygen production in a single stomatal complex following changes in illumination cycles. This work illustrates the flexibility of the SECM technique: Topography and biochemical reactivity can be imaged and a particular location at the sample can be picked to perform kinetic studies of the response to an external stimulus in essentially one experiment.

Yasukawa et al. [86, 99] studied the oxygen production of individual protoblasts from *Bryopsis plumosa* and the response to the administration of several chemicals.

27.2.2.2
Imaging Respiratory Activity via Oxygen Consumption

Oxygen consumption by individual cells or a tissue sample has been detected in a similar way. In this case the UME senses less O_2 in the vicinity of a respiratory-active cell. The investigated systems include HeLa cells [100] and cells from the cell line SW-480 [101]. The respiratory activity was monitored in response to the injection of cell poisons and the kinetics of the uptake of these compounds has been mapped at the single-cell level. Since oxygen is converted at the UME and the living cell, it is crucial to distinguish between a depletion of dissolved O_2 by the respiratory activity of the cell and changes in the working distance d. In a series of papers, Shiku et al. [102, 103] used such measurements to investigate the development of in-vitro-fertilized bovine embryos. In this case the UME was used to perform differential measurements close to the embryo and in the bulk of the culture medium. The respiratory activity was correlated with the survival chances of the embryos. More recently, Matsue and coworkers [85] used specially designed microstructures to cultivate cells from a human erythroleukemia cell line and to measure the O_2 consumption without the problem of protruding cells (Fig. 27.10).

27.2.2.3
Monitoring the Local Release of Signaling Substances

There is a long history of using carbon microelectrodes in detecting the release of neurotransmitters from nerve cells with high temporal resolution [7]. In combination with SECM such experiments could be refined. Hengstenberg et al. [104] used

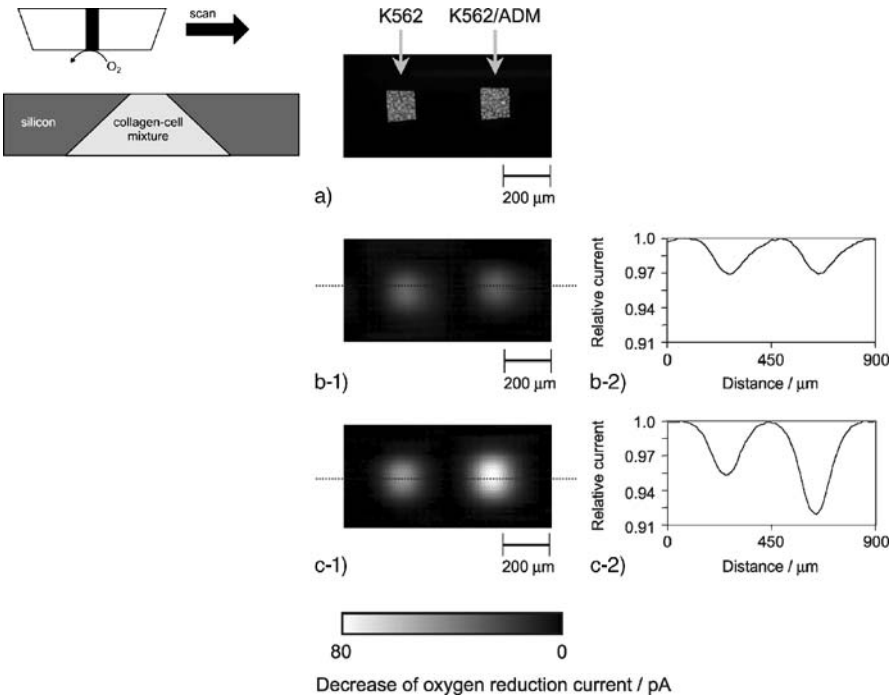

Fig. 27.10. Schematic of the silicon chip for cell assays (*left*) and example of measurements (*right*). (**a**) Optical micrograph of a collagen cell matrix with different human erythroleukemia cell lines incubated in the holes. (**b**) SECM images of oxygen consumption by the cells. Light shades mean high oxygen consumption. (**c**) Same as (**b**) but after 3 days of incubation with 1 µmol l^{-1} adriamycin. One cell line is insensitive to this drug and continues to grow, whereas the respiratory activity of the cell line in the left hole is inhibited. From [85] Copyright 2003, American Chemical Society

carbon-fiber microelectrodes in combination with a shear-force-based SECM system to obtain a low-resolution topographic image of PC12 cells and to position the microelectrode above a specific part of the cell. Upon chemical stimulation with K^+, the release of catechol amines could be monitored without scanning the UME. As the main advantage for using SECM compared to earlier experiments the authors state that the cells are not mechanically stimulated during the microelectrode positioning. In a similar way the release of adrenaline and noradrenaline from single secretory vesicles of chromaffin cells was measured after stimulation [105]. Cells were selected with the help of optical microscopy and the miniaturized carbon electrodes were positioned using a shear-force distance control (see Sect. 27.4).

In a related approach, nitric oxide release from endothelial cells was studied [82]. Among other effects, NO guides the growth of blood capillaries. In order to detect NO, an electrocatalytic sensor with a diameter of 50 µm based on substituted nickel porphyrins was employed. This sensor was combined with a conventional Pt microelectrode (diameter 10 µm) into a dual electrode probe. The Pt electrode was used for positioning the NO sensor close to the surface based on hindered diffusion of

O_2 (27.2). The NO sensor then detected the NO release from the cells. However, to date further miniaturization of the presented NO sensor is limited since the reported currents for the NO detection are in the pA range.

SECM has been used to study the resorption of bone by specialized cells known as osteoclasts [106–108]. Bone is a complex material consisting of calcium-phosphate-based minerals (hydroxyapatite), organic material (mostly collagen) and various cells. The osteoclasts carry out the resorption of bone by the secretion of protons and hydrolytic enzymes, which break down the minerals and proteins releasing, among other species, Ca^{2+} (Fig. 27.11a). Bone is a dynamic system with a balance between the resorption and formation of bone. An imbalance in these processes is involved in many diseases, such as osteoporosis characterized by a loss of bone mineral. Assays for the resorptive activity of the osteoclasts are usually carried out by incubating the cells on bone slices for 18–20 h and then determining the area and number of resorption pits from micrographs. This assay is slow and imprecise. The rate of resorption has been more directly probed using SECM with liquid membrane calcium-selective microelectrodes to determine the Ca^{2+} released from the hydroxyapatite into the culture medium during resorption (Fig. 27.11a). The increase in Ca^{2+} due to the resorptive activity of the cells was detected within approximately 10 min of incubation. The retardation of resorptive activity after fluoride treatment was studied and conclusions about its mechanism were obtained.

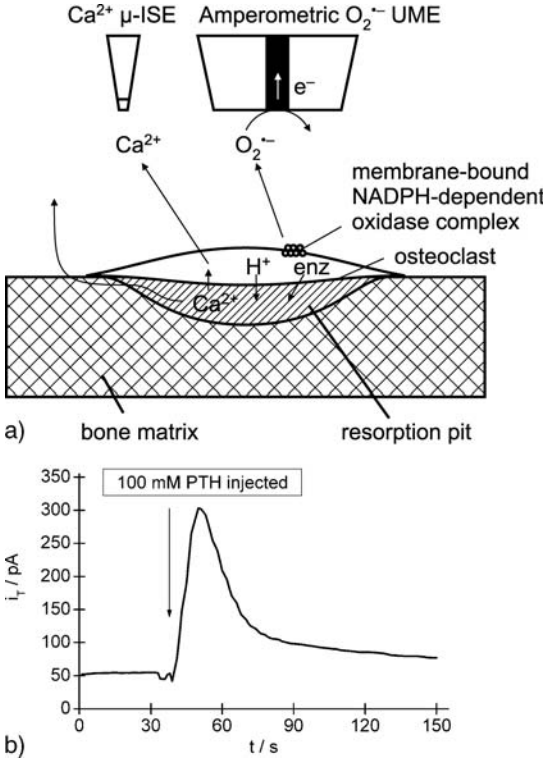

Fig. 27.11. (**a**) Schematic of the processes involved in osteoclastic resorption of bone. Ca^{2+} release can be monitored by a potentiometric Ca^{2+} ion-selective electrode, the superoxide release after stimulation can be recorded by an amperometric electrode. (**b**) Current–time trace for the superoxide release by osteoclasts after stimulation with parathyroid hormone (Reproduced by permission from the Society for Endocrinology from [50])

Free radicals, especially the superoxide anion, are known to be important in the regulation of osteoclast activity and can be detected using an amperometric sensor consisting of cytochrome c covalently attached to a gold electrode [50]. This method was used to detect the acute response of the cells to stimulation by parathyroid hormone (PTH) as a burst of superoxide anion generation. Other work has concentrated on the regulation of the membrane-bound NADPH-dependent oxidase responsible for superoxide generation [50]. The effects of inhibitors of protein kinases, membrane-permeable analogs of cAMP and cholera toxin on the stimulation of superoxide anion production by pertussis toxin (PTH) and ionomycin were studied. cAMP-dependent inhibition was found to be dominant in controlling the superoxide anion production. For this type of collection-mode experiment the SECM apparatus can provide real-time information and can be used in combination with an optical microscope to allow a fast positioning of the UME close to the cells. With such a setup it was demonstrated that the timescale of the superoxide anion burst following the stimulation by PTH was consistent with superoxide diffusion from the osteoclast to the tip (Fig. 27.11b). In contrast to the generally accepted notion of an indirect mediaton of superoxide release by other cells of the osteoblastic lineage, the short timescale of the SECM response together with the observed effects of cholera and pertussis toxins on the superoxide release suggest that the superoxide anion burst results from a direct action of PTH on the osteoclast via a G-protein coupled receptor.

27.2.2.4
Probing the Redox Capacity of Individual Cells

Mirkin et al. [109] demonstrated that the redox recycling of a mediator directly couples to the internal metabolism of metastatic and nonmetastatic human breast cells. Several imaging modes could be demonstrated [109]. Hydrophilic mediators cannot penetrate the lipid cell membrane. An image using these mediators will provide an image of the cell topography based on (27.2). If a redox-active species is distributed inside and outside the cell, electrolysis at the UME may deplete the solution in the vicinity of the biological cell and change the concentration gradient. The cell may respond with a release of this compound and the time trace i_T may be indicative of the transport kinetics of the compound across the cell membrane. The mediator can be regenerated at the cell wall by an incorporated redox system, which shuttles the charge across the cell wall. Finally neutral mediators such as menadione and napthophinone may cross the lipid cell membrane and directly titrate the redox equivalents inside the cell [110]. Feng et al. [111] observed differences between normal and metastatic tumor cells that they related to the different protein expression profiles of the cells. The approach was also expanded to investigate bacteria [112]. The SECM experiments were treated with a theory usually applied for charge transfer occurring at liquid/liquid interfaces. It remains to be demonstrated to which limit such simplifying models can provide a deeper insight into complex internal regulatory processes of cells. Nagamine et al. [113, 114] monitored the metabolic regulation of bacteria that were immobilized within collagen microspots and exposed to osmotic stress. Changing the osmotic conditions changed the permeability of the cell membrane toward the hydrophilic electron mediator $[Fe(CN)_6]^{4-}$. It was found that the SECM

response changed when cells were growing at a medium with D-glucose as the only carbon source. This suggests that the electron flow in the respiratory chain, with which the mediator interferes, depends on the metabolic pathway upstream of the respiratory chain [113].

27.2.3 Investigation of Mass Transport Through Biological Tissue

The SECM response is strongly dependent on the mass transport in the working solution. Therefore, it is conceivable that this technique can be used to image localized mass transport. Localized mass transport occurs in biological tissue, especially increased transport rates may be observed above follicles or pores. Typically, the biological tissue is mounted as a barrier between a donor and an acceptor compartment (Fig. 27.12). The donor compartment contains a redox active species that is driven through the tissue by diffusion (Fig. 27.12a), electroosmosis (Fig. 27.12b), or hydrostatic pressure (Fig. 27.12c) and is detected by the SECM probe in the acceptor compartment in a GC-mode-based configuration. The transport across skin, dentine and the oxygen transport in cartilage were intensively studied. An excellent review on this topic has been published [115]. White and coworkers [116, 117] studied the transport of various species across skin. These are important studies in respect to novel concepts for drug delivery.

The flux models were experimentally verified by studies on synthetic membranes (mica and track-etched membranes). Quantification through an individual pore can be obtained by (27.9)–(27.11). For these investigations the pores are localized in a survey scan, then the UME is directly positioned over a pore center and an approach curve is record. This experimental approach can be fitted to

$$i_{\mathrm{T}}(d) = 4nFDr_{\mathrm{T}}\frac{2c_{\mathrm{S}}}{\pi}\arctan\left(\frac{r_{\mathrm{T}}}{d}\right) . \tag{27.12}$$

Scott et al. [53] identified regions of increased mass transport in hairless mouse skin. It became clear that iontophoretic transport is highly localized and bound to hair follicles. Studies on bulk skin tissues revealed that the transport pathways carry a net negative charge and lead to a preferential transport of cations across skin [118]. The transport of cations induces an electroosmotic flow of the solvent. Therefore the diffusional transport of neutral molecules is modulated by the solvent flow. The relative contributions could be quantified. Figure 27.13 shows the transport of hydroquinone through a single hair follicle of hairless mouse skin by combined diffusion and electroosmotic flow. The skin separates a donor compartment with neutral hydroquinone and a receptor compartment initially not containing hydroquinone. The pure diffusional transport is observed if no iontophoresis current is applied (Fig. 27.13b). If the applied iontophoresis current induces a solvent flow against the diffusional flux

Fig. 27.12. Typical setup for monitoring the transport to biological tissue. The driving force for transport can be provided by a concentration gradient between donor or acceptor compartment (**a**), a current between the donor or acceptor compartment (**b**) or a pressure gradient between the compartments (**c**)

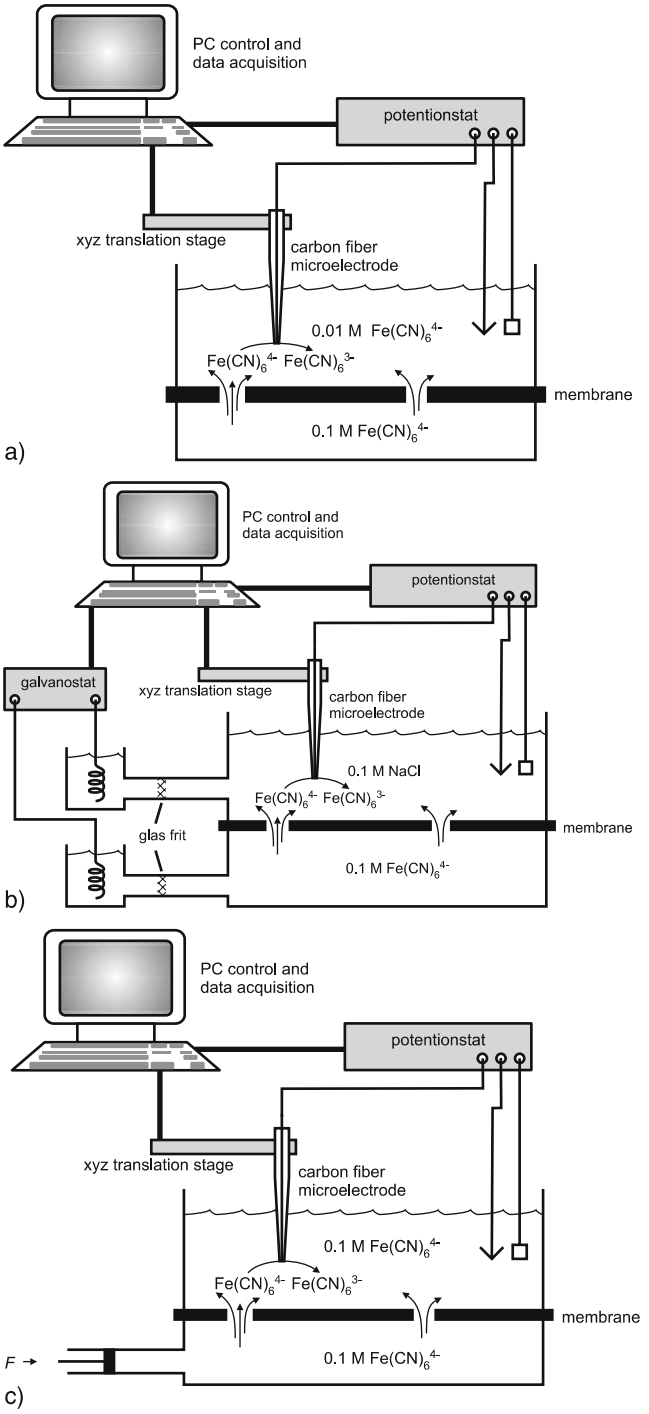
PC control and
data acquisition
potentionstat
xyz translation stage
carbon fiber
microelectrode
0.01 M $Fe(CN)_6^{4-}$
$Fe(CN)_6^{4-}$ $Fe(CN)_6^{3-}$
membrane
0.1 M $Fe(CN)_6^{4-}$
a)
PC control and
data acquisition
potentionstat
galvanostat
xyz translation stage
carbon fiber
microelectrode
0.1 M NaCl
$Fe(CN)_6^{4-}$ $Fe(CN)_6^{3-}$
glas frit
membrane
0.1 M $Fe(CN)_6^{4-}$
b)
PC control and
data acquisition
potentionstat
xyz translation stage
carbon fiber
microelectrode
0.1 M $Fe(CN)_6^{4-}$
$Fe(CN)_6^{4-}$ $Fe(CN)_6^{3-}$
membrane
F →
0.1 M $Fe(CN)_6^{4-}$
c)

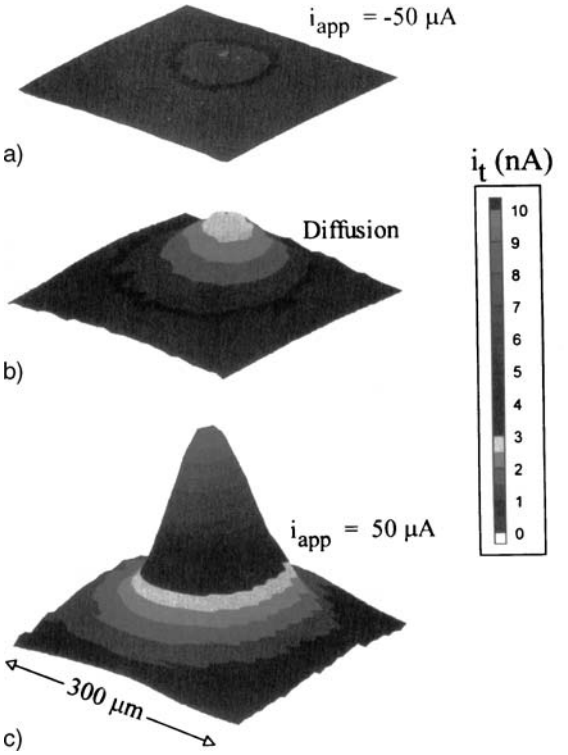

Fig. 27.13. SECM GC images of electroosmotic and diffusional transport of hydroquinone across a single hair follicle in hairless mouse skin. The skins separates a donor compartment with neutral hydroquinone and a receptor compartment that initially does not contain hydroquinone. The *middle image* (**b**) corresponds to pure diffusional transport in the absence of an iontophoresis current. In the *top image* (**a**) the iontophesis current induces a solvent flow from the receptor compartment into the donor compartment, in the *bottom image* (**c**) the current direction is reversed leading to a solvent flow into the receptor compartment. Neutral hydroquinone is transported with the solvent flow and by diffusion. Reprinted with permission from [117], Copyright 2000 Springer

Fig. 27.14. SECM GC images of fluid flow through tubules in dentine. (**a**) Schematic of the experiment. (**b**) SEM image of a dentine slice; (**c**) SECM image of an untreated dentine slice without applied pressure. (**d**) SECM image of an untreated dentine slice with a hydrostatic pressure of 2 kPa to the donor compartment. (**e**) SECM image of a dentine slice after treatment with calcium oxalate without applied pressure. (**f**) SECM image of a dentine slice after treatment with calcium oxalate with a hydrostatic pressure of 2 kPa to the donor compartment. Parts (**c**)–(**f**) reprinted with permission from [120], Copyright 1995 American Chemical Society, Part (**b**) reprinted with permission from [119], Copyright 1996 The Royal Society of Chemistry

(out of the receptor compartment), the transport rate of hydroquinone is decreased (Fig. 27.13a). If the current polarity is reversed so that the solvent with the neutral compounds flows into the receptor compartment, the transport rate is markedly increased (Fig. 27.13c). Changes of transport patterns with differentiation of skin from rats could also be demonstrated.

Dentine is a calcerous material located between the enamel and the pulp of a tooth. It contains pores of 1–2 µm (Fig. 27.14b). Fluid flow inside these tubules is associated with dentinal hypersensitivity. Blocking of this flow is one strategy to treat this condition. Macpherson et al. [119, 120] investigated the convective transport within the tubes. A dentine slice was placed between two electrolyte solutions of identical composition. The UME was used to oxidize $[Fe(CN)_6]^{4-}$ (= Red in Fig. 27.14a). Without any external driving force, the features in the image represent

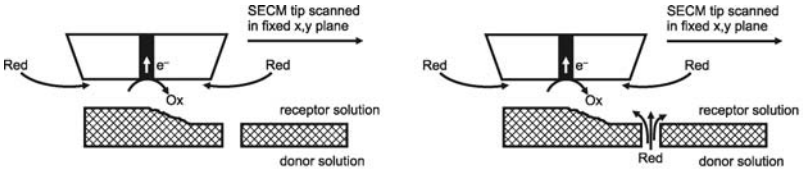

a) without pressure with pressure

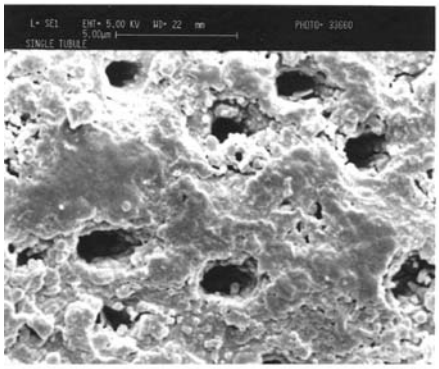

b)

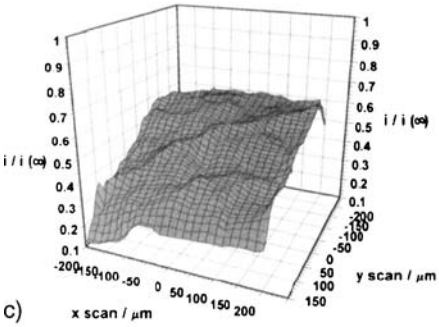

c)

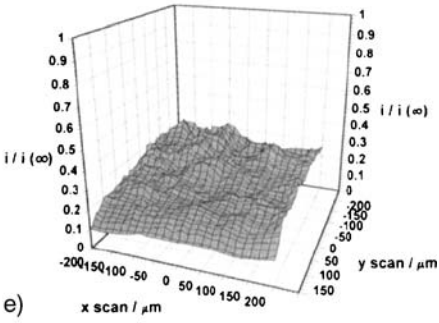

e)

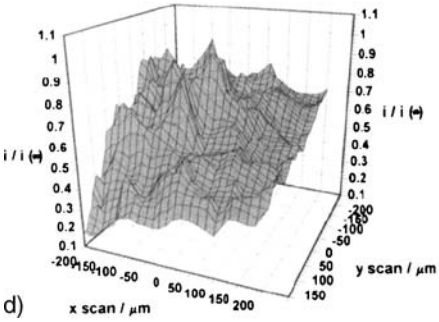

d)

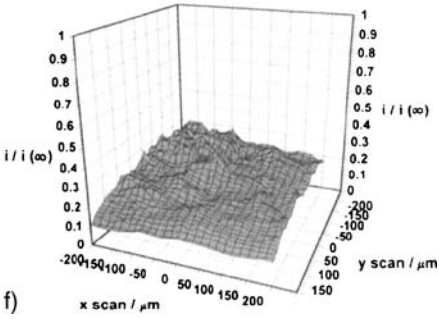

f)

essentially the topographic features of the dentine slice (Fig. 27.14c). By applying a pressure gradient across the dentine slice, a convective flow of the solution can be induced. This leads to increased currents above those dentine pores that are open and to an overall increased level of current (Fig. 27.14d). Treatment of the dentine with calcium oxalate can block the pore by deposition of insoluble calcium oxalate. After such a treatment, there is almost no difference between the images recorded with and without applied hydrostatic pressure (Fig. 27.14e,f). Pure diffusional transport inside dentine was studied by Nugues and Denuault [121]. They could identify occlusions of pores and correlate the current to numerical simulations of pore ensembles.

Experiments similar to the investigation of skin and dentine are also applicable to technical membrane systems.

Mass transport in cartilage was studied by Macpherson and coworkers [122]. Understanding of the redistribution rate of water is central to the load-bearing function of cartilage in the body. The physiological and pathophysiological behavior of cartilage is also related to the transport of oxygen and other nutrients and metabolites by diffusion and convection that can be studied by SECM.

A further increase in the resolution of such measurements and a significantly improved chemical selectivity was demonstrated by Kueng et al. [51,52,123], who integrated an amperometric enzyme sensor into an SFM tip and probed the release of glucose and ATP from artificial membranes under physiologically relevant conditions.

27.3 Application to Technologically Important Electrodes

27.3.1 Investigation of Passive Layers and Local Corrosion Phenomena

27.3.1.1 Detecting Precursor Sites for Pitting Corrosion

SECM can be seen as an ideal tool for corrosion research. It can distinguish between active and passive regions at the sample and detect the concentration of various relevant species such as Fe^{3+}, Fe^{2+}, O_2 and H_2. At most metals a thin oxide layer prevents the continuous dissolution of the metal in aqueous solutions. Local damage of this layer can lead to a rapid local dissolution of the metal while maintaining extreme concentrations of reagents and pH values (pitting corrosion). The initiation of the local breakdown of the passive layers is not yet completely understood. SECM was able to detect precursor sites for pitting corrosion on steel [124–128], Ti [129–133], Ta [134, 135] Ni [136], and Al [137, 138] by their enhanced heterogeneous electron-transfer kinetics to dissolved compounds such as Br^-, I^-, $[Ru(NH_3)_6]^{3+}$, nitrobenzene, etc. The formed reaction products can be detected in the GC mode. On Ti/TiO_2 such regions of enhanced rates of heterogeneous electron transfer turned out to be preferred sites for pitting corrosion under more positive potentials [129, 130]. A significant advantage of the SECM method is its destruction-free character, which allows the identification of precursor sites before the onset of otherwise visible pitting corrosion. By quantification of the fluxes using

(27.10)–(27.12), it was found that 69% of the current at a macroscopic electrode (0.79 cm^2) were passing through 11 precursor regions that totaled only 0.1% of the total area [131]. The precursor site can be associated with inclusions of other elements [133]. Wiliams et al. [139] developed a method to follow the ongoing pit in the vicinity of sulfur-rich inclusions on steel by a combination of complemen-

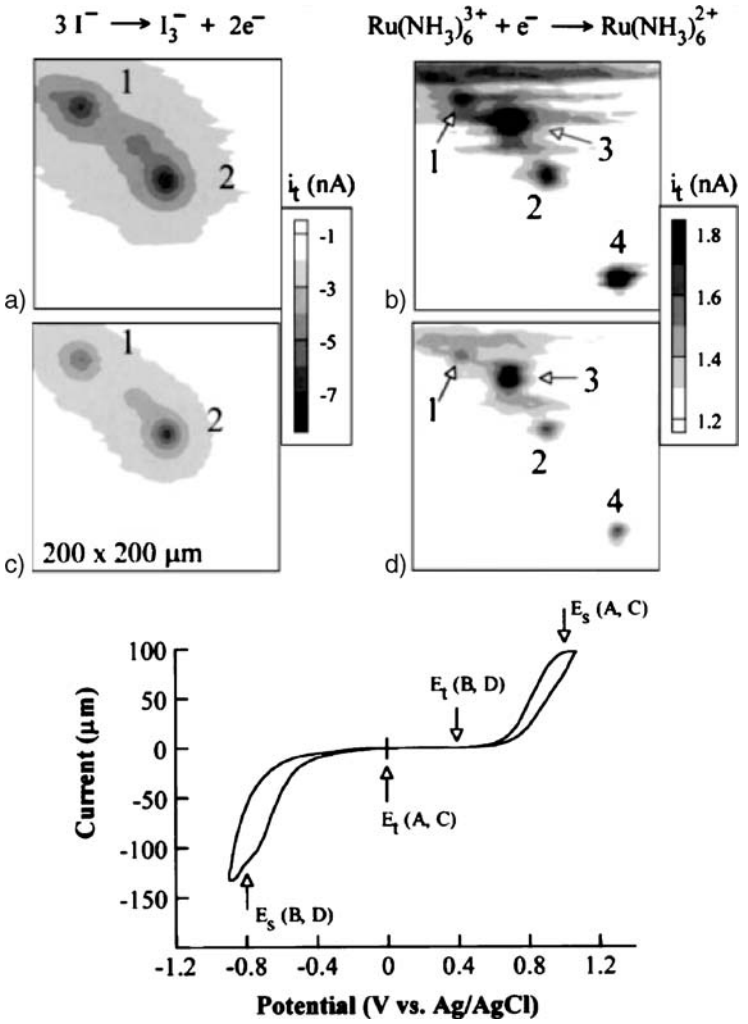

Fig. 27.15. Precursor sites for pitting corrosion on 200 × 200 μm^2 Ta/Ta_2O_5 imaged in the GC mode in a solution containing *both*, 2.5 mM $[Ru(NH_3)_6]^{3+}$ and 10 mM I^-. Oxidation of I^- (**a**) proceeds at sites 1 and 2 only, $E_S = 1.0$ V, $E_T = 0.0$ V. Reduction of $[Ru(NH_3)_6]^{3+}$ (**b**) is found on sites 1–4 ($E_S = -0.8$ V, $E_T = +0.4$ V). By changing E_S and E_T it was switched repeatedly between images such as that shown in (**a**) or in (**b**). The cyclic voltammogram of the macroscopic electrode (**c**) shows the sum of the reaction at all sites and does not reveal the chemical selectivity of the sites; $v = 20\,mV\,s^{-1}$, ordinate label should be "Current (µA)" [G.W.]. Reprinted with permission from [135], Copyright 1999 American Chemical Society

tary microscopic techniques. Sulfur species were locally detected by reaction of microelectrode-generated I_3^- [125, 140]. SECM could demonstrate that SiC particles are preferred sites for oxygen reduction at Al-based composite material [141]. For inclusion-free materials, the structural nature of the precursor sites could not yet be determined. Passive layers of different metals show interesting differences. While Ti/TiO_2 has no chemical sensitivity with respect to dissolved compounds, precursor sites on Ta/Ta_2O_5 showed a remarkably different sensitivity towards I^- and $[Ru(NH_3)_6]^{3+}$ (Fig. 27.15) [135] When the sample was held at $E_S = 1.0\,V$ (oxidation of I^-) and the UME at $E_T = 0.0\,V$ (reduction of I_3^-), two sample regions that could oxidize I^- became visible (Fig. 27.15a,c). When the sample was held at $E_S = -0.8\,V$ in order to reduce $[Ru(NH_3)_6]^{3+}$ and the UME was held at $E_T = +0.4$ (oxidation of $[Ru(NH_3)_6]^{2+}$), four regions were detected at which electron transfer occurred at the sample (Fig. 27.15b,d). By changing E_S and E_T it was switched repeatedly between images.

27.3.1.2
Triggering and Monitoring of Active Local Corrosion

Pitting corrosion can be triggered locally by high chloride concentrations. SECM has been used to produce locally high chloride concentrations by reduction of trichloroacetic and dichloroactetic acids and to follow the subsequent development of the pit over time [142, 143].

SECM has also been used to monitor active corrosion processes either by identification of corrosion products by cyclic voltammetry at the UME, or by the use of potentiometric ion-selective electrodes. Besides steel [144], examples include dental fillings from amalgams and metallic implants [145, 146], titanium [147], alloys [148–154], potentiometric sensor materials of AgI [155], silicon in etching solutions [156], organic coatings [157, 158], enzyme–mediator–graphite composite materials for amperometric biosensors [159], and diamond-like carbon-coated optical waveguides from zinc selenide [160].

Different passivating properties of crystallites on Ti/TO_2 have been identified with the feedback mode of the SECM [161]. The crystallites could be clearly identified by their different heterogeneous kinetics for the $[Fe(CN)_6]^{3-}$ reduction. The pattern correlated with the crystallites detected in optical microscopy [147].

A new approach that currently emerges is the use of an AC signal at the microelectrode. Although the nature of such signals is currently still under discussion [162], it turned out to be useful for detecting small defects in technical materials and coatings [93, 151, 163].

27.3.2
Investigation of Electrocatalytically Important Electrodes

SECM has recently attracted a lot of attention as a tool to investigate electrocatalytically important electrodes connected to the development of fuel cells. The electrochemical hydrogen-oxidation reaction (HOR) and the oxygen-reduction reaction (ORR) are both electrocatalytical reactions. Technically, many problems are

associated with catalytic materials. They are sensitive to poisoning by other compounds, and Pt-based catalysts are of limited availability. Therefore, alloys need to be tested that could replace or complement Pt-based catalysts.

27.3.2.1 Investigation of Hydrogen-Oxidation Reaction

The HOR reaction has been studied in the GC and feedback mode [164–168]. The H^+/H_2 redox couple was used as mediator. Unlike outer-sphere redox couples that have been discussed previously, the kinetics of the H^+/H_2 strongly depend on the catalytic properties of the electrode. In a typical experiment H^+ is reduced at the UME and the formed H_2 is then oxidized at the sample that is held at a specific potential. By evaluating approach curves according to (27.2)–(27.6) the potential-dependent kinetics of the HOR at the sample could be reconstructed [164]. The measurements are carried out in a steady-state regime. This is advantageous because the response is comparatively free of interferences common in alternative experiments and caused by ohmic drop, double-layer charging currents or mechanical difficulties associated with cyclic voltammetry at high scan rates or rotating-disk experiments, respectively.

27.3.2.2 Investigation of Oxygen-Reduction Reaction

The ORR is a complicated multistep reaction. In a still simplified version at least three reactions have to be considered in acidic solution

$$O_2 + 2e^- + 2H^+ \rightarrow H_2O_2 \tag{27.13}$$

$$H_2O_2 + 2e^- + 2H^+ \rightarrow 2H_2O\,, \tag{27.14}$$

$$O_2 + 4e^- + 4H^+ \rightarrow 2H_2O\,. \tag{27.15}$$

The rates of these reactions are also very dependent on the electrode material. The reaction is investigated in the tip-generation/substrate collection mode (TG/SC, Fig. 27.2b) [169–171]. Specifically, the UME is placed in proximity to the sample and molecular oxygen is produced by applying a constant current at the UME in acidic medium (Fig. 27.16). The oxygen diffuses to the sample and is reduced there. By plotting the sample current vs. the UME position, a mapping of the electrocatalytic efficiency is obtained. This has been used to scan chips at which electrocatalysts of systematically varied composition were prepared by combinatorial methods [169] (Fig. 27.17). The different spots represent different total compositions of the system Pd-Au-Co. The relative composition at each catalyst spot can be obtained by projecting three lines from an individual spot as indicated by the arrows in the lower-right part of each panel to the three axes for the composition (in atomic ratio). The bright spots are obtained for those material combinations that are effective oxygen-reduction catalysts. Potential-dependent properties can be obtained by performing the experiment with different substrate potentials. In contrast to the feedback mode, the TG/SC mode does not require that the product of the reaction at the sample

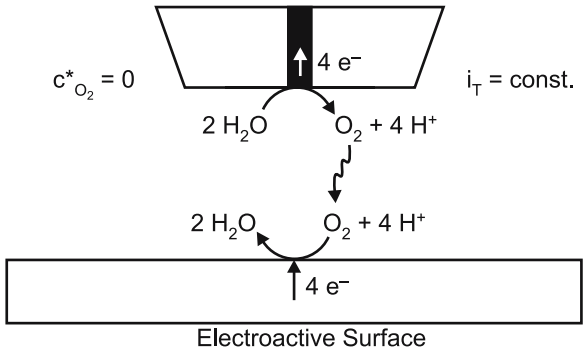

Fig. 27.16. Scheme of the TG/SC mode for the investigation of ORR as used in [169, 171]

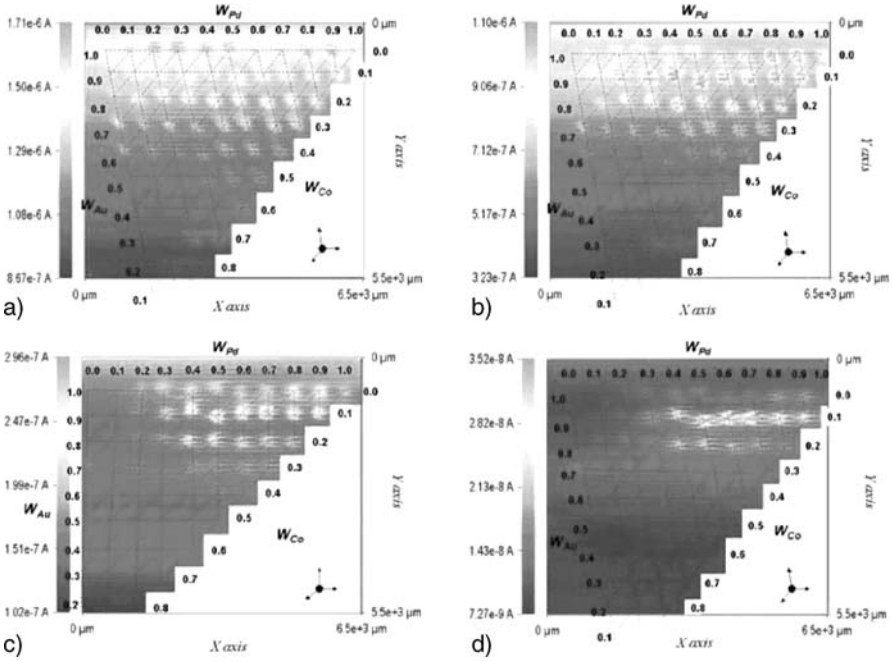

Fig. 27.17. SECM TG/SC images of oxygen reduction activity measured on Pd-Au-Co arrays in 0.5 M H_2SO_4. $d = 30\,\mu m$, constant UME current $= +160$ nA, $E_S = 0.2$ (**a**), 0.4 (**b**), 0.6 (**c**), 0.7 (**d**) V vs. HRE. W_M is the atomic ratio of the metal M in the spot. Reprinted with permission from [169], Copyright 2005 American Chemical Society

diffuses back to the UME to close the chemical feedback loop. This allows the investigation of irreversible reactions such as ORR. ORR in alkaline medium around pH 12 can also be investigated in the feedback mode [172]. Hydroxide ions serve as mediator. They are oxidized to O_2 at the UME and O_2 is reduced to OH^- at a platinum sample. The applicability of this mode is not only limited by the narrow pH range but also by the fact that many metal samples will give H_2O_2 as one of the reduction products at the sample.

27.4 Conclusion and Outlook: New Instrumental Developments and Implication for Future Applications

SECM has been applied to study a large variety of heterogeneous reactions at solid/liquid interfaces. The examples of high practical relevance include studies of corrosion mechanisms of passivated metals, heterogeneous catalysis for fuel-cell materials, catalysis by immobilized enzymes used in biosensors and metabolic activity of single cells and intact organs. The SECM image provides a direct representation of interfacial reactivity even in those cases when the topography of the interface does not changes during the reaction, e.g. during an electron transfer from an electrode to a dissolved compound without accompanying deposition or dissolution processes. Furthermore, detailed kinetic analysis can be obtained by recording approach curves and by fitting the data to models of the interfacial reaction and mass-transfer processes. This ability has largely been exploited in fundamental electrochemistry, however, it was not the focus of this review. Finally, the possibility to modify surfaces by a large variety of chemically *well-defined* surface modifications holds a great potential for prototyping of advanced functional surfaces.

Currently, there are perhaps two main obstacles for a broader application of the technique: First, the lateral resolution and secondly, the level of fundamental knowledge in electrochemistry required to perform successful SECM experiments. Most studies have been performed in the micrometer range for a number of reasons: i) Preparation and characterization of electrodes with defined geometry is challenging for electrodes smaller than 1 μm. Such electrodes are required for quantitative work. ii) The working distance is proportional to r_T in the feedback mode. For submicrometer probes, a constant-distance working mode is required (vide infra). iii) The relevant effects are bound to the micrometer dimension (biological cells, biosensor arrays). Of course, there is a need for higher lateral resolution, in particular for a broader application in material science, where the investigation of reactions at individual grain boundaries would be an important objective.

Therefore, many attempts are currently being made to improve the lateral resolution and to ease the operation of SECM instruments and data interpretation. Highly desirable are mechanisms for guiding an UME over protruding samples. This requires a signal that is independent of the measured current (because the current is strongly influenced by the chemical properties of the sample). Most promising are methods based on shear forces (vide supra). Another development is to integrate UME or other chemical sensors into SFM tips or to combine other complementing scanning probe techniques. This direction is covered in the Chapt. 8 by Kranz of this volume. When discussing future possibilities to increase the lateral resolution, one should keep in mind some limitations for optimization. In the GC mode the resolution is controlled by the diffusion field of the active *sample* regions. A large active region will make it impossible to resolve small features in its vicinity even with a very small probe. In the feedback mode, the resolution is primarily controlled by the size of the active UME area. Besides this, the working distance and the size of the insulating shielding have a considerable influence. The smaller the working distance the better the achievable lateral resolution. Since the normalized distance is important, the working distance has to be reduced proportionally to the UME radius.

This makes it clear why current-independent distance-control schemes are the main prerequisite for enhancing resolution. The insulating shielding should be as thin as possible for high lateral resolution [173]. However, the smaller the insulating shielding the lower the sensitivity, which is also important for detecting small features on the sample. In many cases compromises have to be found for specific problems. The sensitivity is also significantly influenced by the kinetics at the sample and that adds another fundamental limitation to lateral resolution. Consider Fig. 27.3, curve 3. This curve represents a case where the reactivity of the sample surface can just be distinguished from an inert, insulating matrix. It corresponds to a normalized rate constant $\kappa = k_{\mathrm{eff}} r_{\mathrm{T}}/D = 0.3$. Since diffusion coefficients in aqueous solution do not vary too much, one can make a simple estimate, what is the minimum heterogeneous rate constant that must be present at the sample so that a contrast in an image is obtained using a UME of a specific r_{T} (Table 27.3). At an $r_{\mathrm{T}} = 5$ nm, the reaction rate constant at the sample must be as high as $3\,\mathrm{cm\,s^{-1}}$ that it corresponds to an almost diffusion-controlled reaction at conventional electrodes! SECM will become "blind" to all slower reactions at this UME size. While considerable progress has been reported to fabricate such UME, e.g. in Refs. [174, 175], the time for successful imaging experiments with them is still to come. However, imaging with electrodes of $r_{\mathrm{T}} \approx 50$ nm seems realistic for selected samples [174, 175]. Considering the interdependence of image features and heterogeneous chemical kinetics, it becomes clear that the strength of SECM will be imaging of chemical reactions. Therefore, the size of the electrode needs to be selected according to the investigated problem and despite the exciting progress, which can be achieved with nanometer-sized electrodes, there will still be many applications using micrometer-sized electrodes. Issues of resolution cannot be discussed independently of the sample and the reaction to be studied.

Table 27.3. Required heterogeneous rate constant k_{eff} to result in an approach curve such as curve 3 ($\kappa = 0.3$) in Fig. 27.3. $D = 5 \times 10^{-6}\,\mathrm{cm\,s^{-1}}$

$r_{\mathrm{T}}/\mu\mathrm{m}$	12.5	5	1	0.5	0.1	0.05	0.025	0.005
$k_{\mathrm{eff}}/\mathrm{cm\,s^{-1}}$	0.0012	0.003	0.015	0.03	0.15	0.3	0.6	3

Acknowledgements. The work on SECM in the authors' laboratory has been supported over the years by Deutsche Forschungsgemeinschaft, the State of Lower Saxony, the VW Foundation, the Alexander von Humboldt Foundation, the Fonds of the Chemical Industries and the Hanse Institute of Advanced Studies. G.W. would like to express sincere thanks to the University of Oldenburg for granting a sabbatical semester and in particular to Carl H. Hamann for taking up the teaching load during that time! We are grateful for the critical comments of our colleagues C. Kranz (Georgia Institute of Technology), I. Zawisza and A. Kittel (University of Oldenburg) that helped to improve the manuscript. The authors are thankful to A.J. Bard, T. Matsue, H. Shiku, H.S. White, J. Macpherson, and P. Unwin for supplying electronic versions of the original figures for this review.

References

1. Bard AJ, Mirkin MV (eds) (2001) Scanning Electrochemical Microscopy. Marcel Dekker, Inc., New York, Basel

2. Barker AL, Gonsalves M, Macpherson JV, Slevin CJ, Unwin PR (1999) Anal Chim Acta 385:223
3. Wittstock G (2003) Imaging Localized Reactivities of Surfaces by Scanning Electrochemical Microscopy. In: Wandelt K, Thurgate S (eds) Solid-Liquid Interfaces, Macroscopic Phenomena - Microscopic Understanding. Springer-Verlag, Berlin, Heidelberg, p 335
4. Wittstock G (2001) Fresenius J Anal Chem 370:303
5. Horrocks BR (2003) Scanning Electrochemical Microscopy. In: Unwin PR (ed) Instrumentation and Electroanalytical Chemistry. Wiley-VCH, Weinheim, p 444
6. Fleischmann M, Stanley P, Rolison DR, Schmidt PP (1987) Ultramicroelectrodes. Datatech Systems, Inc., Morganton, NC
7. Adams RN (1990) Prog Neurobiol 35:297
8. Engstrom RC, Weber M, Wunder DJ, Burges R, Winquist S (1986) Anal Chem 58:844
9. Liu H-Y, Fan F-RF, Lin CW, Bard AJ (1986) J Am Chem Soc 108:3838
10. Kwak J, Bard AJ (1989) Anal Chem 61:1794
11. Bard AJ, Fan F-RF, Kwak J, Lev O (1989) Anal Chem 61:132
12. Oesterschulze E, Abelmann L, van den Bos A, Kassing R, Schwendler N, Wittstock G, Ziegler C (2006) Sensor Technology for Scanning Probe Microscopy and New Applications. In: Bhushan B, Fuchs H, Kawata S (eds) Applied Scanning Probe Methods II. Springer, Berlin, Heidelberg, New York,
13. Saito Y (1968) Rev Polarogr (Jpn) 15:177
14. Amphlett JL, Denuault G (1998) J Phys Chem B 102:9946
15. Bard AJ, Mirkin MV, Unwin PR, Wipf DO (1992) J Phys Chem 96:1861
16. Bard AJ, Fan F-RF, Pierce DT, Unwin PR, Wipf DO, Zhou F (1991) Science 254:68
17. Wang J, Wu L-H, Li R (1989) J Electroanal Chem 272:285
18. Horrocks BR, Wittstock G (2001) Biological Systems. In: Bard AJ, Mirkin MV (eds) Scanning Electrochemical Microscopy. Marcel Dekker, New York, Basel, p 445
19. Shiku H, Ohya H, Matsue T (2002) Encyclop Electrochem 9:257
20. Zhao C, Wittstock G (2004) Anal Chem 76:3145
21. Anthony C (1996) Biochem J 320:697
22. Ye L, Haemmerle M, Olsthoorn AJJ, Schuhmann W, Schmidt HL, Duine JA, Heller A (1993) Anal Chem 65:238
23. Nistor C, Rose A, Wollenberger U, Pfeiffer D, Emneus J (2002) Analyst 127:1076
24. Wijayawardhana CA, Wittstock G, Halsall HB, Heineman WR (2000) Anal Chem 72:333
25. Pierce DT, Unwin PR, Bard AJ (1992) Anal Chem 64:1795
26. Kranz C, Wittstock G, Wohlschläger H, Schuhmann W (1997) Electrochim Acta 42:3105
27. Pierce DT, Bard AJ (1993) Anal Chem 65:3598
28. Shiku H, Takeda T, Yamada H, Matsue T, Uchida I (1995) Anal Chem 67:312
29. Shiku H, Matsue T, Uchida I (1996) Anal Chem 68:1276
30. Wittstock G, Wilhelm T, Bahrs S, Steinrücke P (2001) Electroanalysis 13:669
31. Zaumseil J, Wittstock G, Bahrs S, Steinrücke P (2000) Fresenius J Anal Chem 367:352
32. Kwak J, Bard AJ (1989) Anal Chem 61:1221
33. Wei C, Bard AJ, Mirkin MV (1995) J Phys Chem 99:16033
34. Mirkin MV, Arca M, Bard AJ (1993) J Phys Chem 97:10790
35. Mirkin MV, Fan F-RF, Bard AJ (1992) J Electroanal Chem 328:47
36. Zhao C, Sinha JK, Wijayawardhana CA, Wittstock G (2004) J Electroanal Chem 561:83
37. Wilhelm T, Wittstock G (2000) Mikrochim Acta 133:1
38. Wittstock G, Schuhmann W (1997) Anal Chem 69:5059
39. Horrocks BR, Schmidtke D, Heller A, Bard AJ (1993) Anal Chem 65:3605
40. Horrocks BR, Mirkin MV, Pierce DT, Bard AJ, Nagy G, Toth K (1993) Anal Chem 65:1213
41. Horrocks BR, Mirkin MV (1998) J Chem Soc 94:1115
42. Shiku H, Hara Y, Matsue T, Uchida I, Yamauchi T (1997) J Electroanal Chem 438:187

43. Wilhelm T, Wittstock G (2001) Electrochim Acta 47:275
44. Zhao C, Wittstock G (2005) Biosens Bioelectron 20:1277
45. Wijayawardhana CA, Wittstock G, Halsall HB, Heineman WR (2000) Electroanalysis 12:640
46. Wittstock G, Jenkins SH, Halsall HB, Heineman WR (1998) Nanobiology 4:153
47. Wittstock G, Yu K-j, Halsall HB, Ridgway TH, Heineman WR (1995) Anal Chem 67:3578
48. Zhao C, Wittstock G (2004) Angew Chem Int Ed Engl 43:4170
49. Antonenko YN, Pohl P, Rosenfeld E (1996) Arch Biochem Biophys 333:225
50. Berger CEM, Horrocks BR, Datta HK (1998) J Endocrinology 158:311
51. Kueng A, Kranz C, Mizaikoff B (2005) Biosens Bioelectron 21:346
52. Kueng A, Kranz C, Lugstein A, Bertagnolli E, Mizaikoff B (2005) Angew Chem, Int Ed 44:3419
53. Scott ER, White HS, Phipps JB (1993) Anal Chem 65:1537
54. Scott ER, White HS, Phipps JB (1991) J Membr Sci 58:71
55. Nowall WB, Dontha N, Kuhr WG (1998) Biosens Bioelectron 13:1237
56. Rosenwald SE, Dontha N, Kuhr WG (1998) Anal Chem 70:1133
57. Tiefenauer LX, Padeste C (1999) Chimia 53:62
58. Mandler D, Meltzer S, Shohat I (1996) Israel J Chem 36:73
59. Mandler D (2001) Micro- and Nanopatterning using the Scanning Electrochemical Microscope. In: Bard AJ, Mirkin MV (eds) Scanning Electrochemical Microscopy. Marcel Dekker, New York, Basel, p 593
60. Tenent RC, Wipf DO (2003) J Electrochem Soc 150:E131
61. Nowall WB, Wipf DO, Kuhr WG (1998) Anal Chem 70:2601
62. Kranz C, Gaub HE, Schuhmann W (1996) Adv Mater 8:634
63. Wilhelm T, Wittstock G (2003) Angew Chem Int Ed 42:2247
64. Sauter S, Wittstock G (2001) J Solid State Electrochem 5:205
65. Torisawa YSY-S, Shiku H, Yasukawa T, Nishizawa M, Matsue T (2005) Biomaterials 26:2165
66. Shiku H, Uchida I, Matsue T (1997) Langmuir 13:7239
67. Oyamatsu D, Kanaya N, Shiku H, Nishizawa M, Matsue T (2003) Sensors And Actuators B B91:199
68. Kaya T, Nagamine K, Matsui N, Yasukawa T, Shiku H, Matsue T (2004) Chem Commun, p 248
69. Ogasawara D, Hirano Y, Yasukawa T, Shiku H, Matsue T, Kobori K, Ushizawa K, Kawabata S (2004) Chem Sens 20:139
70. Motochi N, Hirano Y, Abiko Y, Oyamatsu D, Nishizawa M, Matsue T, Ushizawa K, Kawabata S (2002) Chem Sens 18:172
71. Kasai S, Yokota A, Zhou H, Nishizawa M, Onouchi T, Niwa K, Matsue T (2000) Anal Chem 72:5761
72. Wijayawardhana CA, Ronkainen-Matsuno NJ, Farrel SM, Wittstock G, Halsall HB, Heineman WR (2001) Anal Sci 17:535
73. Wang J, Song F, Zhou F (2002) Langmuir 18:6653
74. Carano M, Lion N, Abid J-P, Girault HH (2004) Electrochem Commun 6:1217
75. Wang J, Zhou F (2002) J Electroanal Chem 537:95
76. Turcu F, Schulte A, Hartwich G, Schuhmann W (2004) Angew Chem Int Ed Engl 43:3482
77. Turcu F, Schulte A, Hartwich G, Schuhmann W (2004) Biosens Bioelectron 20:925
78. Fortin E, Mailley P, Lacroix L, Szunerits S (2006) Analyst
79. Kranz C, Ludwig M, Gaub HE, Schuhmann W (1995) Adv Mater 7:38
80. Szunerits S, Knorr N, Calemczuk R, Livache T (2004) Langmuir 20:9236
81. Tsionsky M, Cardon ZG, Bard AJ, Jackson RB (1997) Plant Physiol 113:895
82. Isik S, Etienne M, Oni J, Bloechl A, Reiter S, Schuhmann W (2004) Anal Chem 76:6389

83. Torisawa Y-S, Shiku H, Kasai S, Nishizawa M, Matsue T (2004) Int J Cancer 109:302
84. Torisawa Y-S, Shiku H, Kasai S, Nishizawa M, Matsue T (2003) Chem Sens 19:28
85. Torisawa Y-S, Kaya T, Takii Y, Oyamatsu D, Nishizawa M, Matsue T (2003) Anal Chem 75:2154
86. Yasukawa T, Kaya T, Matsue T (1999) Anal Chem 71:4631
87. James P, Garfias-Mesias LF, Moyer PJ, Smyrl WH (1998) J Electrochem Soc 145:64
88. Hirano Y, Oyamatsu D, Yasukawa T, Shiku H, Matsue T (2004) Electrochemistry (Tokyo) 72:137
89. Lee Y, Bard AJ (2002) Anal Chem 74:3626
90. Yamada H, Fukumoto H, Yokoyama T, Koike T (2005) Anal Chem 77:1785
91. Ludwig M, Kranz C, Schuhmann W, Gaub HE (1995) Rev Sci Instrum 66:2857
92. Brunner R, Bietsch A, Hollenricher O, Marti O (1997) Rev Sci Instrum 68:1769
93. Etienne M, Schulte A, Schuhmann W (2004) Electrochem Commun 6:288
94. Etienne M, Schulte A, Mann S, Jordan G, Dietzel ID, Schuhmann W (2004) Anal Chem 76:3682
95. Bauermann LP, Schuhmann W, Schulte A (2004) Phys Chem Chem Phys 6:4003
96. Ballesteros Katemann B, Schulte A, Schuhmann W (2004) Electroanalysis 16:60
97. Ballesteros Katemann B, Schulte A, Schuhmann W (2003) Chem Eur J 9:2025
98. Hengstenberg A, Blöchl A, Dietzel ID, Schuhmann W (2001) Angew Chem Int Ed Engl 40:905
99. Yasukawa T, Kaya T, Matsue T (1999) Chem Lett 9:975
100. Nishizawa M, Takoh K, Matsue T (2002) Langmuir 18:3645
101. Yasukawa T, Kondo Y, Uchida I, Matsue T (1998) Chem Lett 767
102. Shiku H, Shiraishi T, Aoyagi S, Utsumi Y, Matsudaira M, Abe H, Hoshi H, Kasai S, Ohya H, Matsue T (2004) Anal Chim Acta 522:51
103. Shiku H, Shiraishi T, Ohya H, Matsue T, Abe H, Hoshi H, Kobayashi M (2001) Anal Chem 73:3751
104. Hengstenberg A, Blöchl A, Dietzel ID, Schuhmann W (2001) Angew Chem Int Ed 40:905
105. Pitta Bauermann L, Schuhmann W, Schulte A (2004) Phys Chem Chem Phys 6:4003
106. Berger CEM, Rathod H, Gillespie JI, Horrocks BR, Datta HK (2001) J Bone Miner Res 16:2092
107. Berger CEM, Horrocks BR, Datta HK (1999) Molec Cellular Endocrin 149:53
108. Berger CEM, Horrocks BR, Datta HK (1999) Electrochim Acta 44:2677
109. Liu B, Rotenberg SA, Mirkin MV (2000) Proc Natl Acad Sci USA 97:9855
110. Liu B, Rotenberg SA, Mirkin MV (2002) Anal Chem 74:6340
111. Feng W, Rotenberg SA, Mirkin MV (2003) Anal Chem 75:4148
112. Liu B, Cheng W, Rotenberg SA, Mirkin MV (2001) J Electroanal Chem 500:590
113. Nagamine K, Matsui N, Kaya T, Yasukawa T, Shiku H, Nakayama T, Nishino T, Matsue T (2005) Biosens Bioelectron 21:145
114. Nagamine K, Kaya T, Yasukawa T, Shiku H, Matsue T (2005) Sens Actuators B B108:676
115. Bath BD, White HS, Scott ER (2001) Imaging Molecular Transport Across Membranes. In: Bard AJ, Mirkin MV (eds) Scanning Electrochemical Microscopy. Marcel Dekker, New York, Basel, p 343
116. Bath BD, Scott ER, Phipps JB, White HS (2000) J Pharm Sci 89:1537
117. Bath BD, White HS, Scott ER (2000) Pharmaceut Res 17:471
118. Burnette RR, Marrero D (1986) J Pharm Sci 85:1186
119. Macpherson JV, Beeston MA, Unwin PR, Hughes NP, Littlewood D (1995) J Chem Soc Faraday Trans I 91:1407
120. Macpherson JV, Beeston MA, Unwin PR, Hughes NP, Littlewood D (1995) Langmuir 11:3959
121. Nugues S, Denuault G (1996) J Electroanal Chem 408:125

122. Gonsalves M, Barker AL, Macpherson JV, Unwin PR, O'hare D, Winlove PC (2000) Biophysical Journal 78:1578
123. Kueng A, Kranz C, Mizaikoff B (2004) Biosens Bioelectron 19:1301
124. Zhu Y, Williams DE (1997) J Electrochem Soc 144:43
125. Lister TE, Pinhero PJ (2003) Electrochim Acta 48:2371
126. Lister TE, Pinhero PJ (2005) Anal Chem 77:2601
127. Tanabe H, Yamamura Y, Misawa T (1995) Mater Sci Forum 185-188:991
128. Luong BT, Nishikata A, Tsuru T (2003) Electrochemistry 71:555
129. Casillas N, Charlebois SJ, Smyrl WH, White HS (1994) J Electrochem Soc 141:636
130. Casillas N, Charlebois SJ, Smyrl WH, White HS (1993) J. Electrochem. Soc. 140:142
131. Basame SB, White HS (1998) J Phys Chem B 102:9812
132. Basame SB, White HS (1995) J Phys Chem 99:16430
133. Garfias-Mesias LF, Alodan M, James P, Smyrl WH (1998) J Electrochem Soc 145:2005
134. Basame SB, White HS (1999) Anal Chem 71:3166
135. Basame SB, White HS (1999) Langmuir 15:819
136. Paik C–H, Alkire RC (2001) J Electrochem Soc 148:B276
137. Serebrennikova I, Lee S, White HS (2002) Faraday Discuss 121:199
138. Serebrennikova I, White HS (2001) Electrochem Solid State Lett 4:4
139. Williams DE, Mohiuddin TF, Zhu YY (1998) J Electrochem Soc 145:2664
140. Paik C–H, White HS, Alkire RC (2000) J Electrochem Soc 147:4120
141. Pech-Canul MA, Pech-Canul MI, Wipf DO (2004) J Electrochem Soc 151:B299
142. Still JW, Wipf DO (1997) J Electrochem Soc 144:2657
143. Wipf DO (1994) Colloid Surf A 93:251
144. Tanabe H, Togashi K, Misawa T, Mudali UK (1998) J Mater Sci Lett 17:551
145. Gilbert JL, Zarka L, Chang E, Thomas CH (1998) J Biomed Mater Res 42:321
146. Gilbert JL, Smith SM, Lautenschlager EP (1993) J Biomed Mater Res 27:1357
147. Fushimi K, Okawa T, Azumi K, Seo M (2000) J Electrochem Soc 147:524
148. Park JO, Paik C–H, Alkire RC (1996) J Electrochem Soc 143:174
149. Seegmiller JC, Buttry AD (2003) J Electrochem Soc 150:B413
150. Schulte A, Belger S, Etienne M, Schuhmann W (2004) Mater Sci Eng A A378:523
151. Belger S, Schulte A, Hessing C, Pohl M, Schuhmann W (2004) Materialwiss Werkst 35:276
152. Schulte A, Belger S, Schuhmann W (2002) Mater Sci Forum 394-395:145
153. Davoodi A, Pan J, Leygraf C, Norgren S (2005) Electrochem Solid State Lett 8:B21
154. Lister TE, Pinhero PJ, Towbridge TL, Mizia RE (2005) J Electrochem Soc 579:291
155. Toth K, Nagy G, Horrocks BR, Bard AJ (1993) Anal Chim Acta 282:239
156. Shreve GA, Karp CD, Pomykal KE, Lewis NS (1995) J Phys Chem 99:5575
157. Ballesteros Katemann B, Inchauspe CG, Castro PA, Schulte A, Calvo EJ, Schuhmann W (2003) Electrochim Acta 48:1115
158. Bastos AC, Simoes AM, Gonzalez S, Gonzalez-Garcia Y, Souto RM (2005) Prog Org Coat 53:177
159. Gründig B, Wittstock G, Rüdel U, Strehlitz B (1995) J Electroanal Chem 395:143
160. Janotta M, Rudolph D, Kueng A, Kranz C, Voraberger H-S, Waldhauser W, Mizaikoff B (2004) Langmuir 20:8634
161. Fushimi K, Okawa T, Seo M (2000) Electrochemistry 68:950
162. Baranski AS, Diakowski PM (2004) J Solid State Electrochem 8:683
163. Ballesteros Katemann B, Schulte A, Calvo EJ, Koudelka-Hep M, Schuhmann W (2002) Electrochem Commun 4:134
164. Jambunathan K, Shah BC, Hudson JL, Hillier AC (2001) J Electroanal Chem 500:279
165. Shah BC, Hillier AC (2000) J Electrochem Soc 147:3043
166. Zhou J, Zu Y, Bard AJ (2000) J Electroanal Chem 491:22

167. Ahmed S, Ji S, Petrik L, Linkov VM (2004) Anal Sci 20:1283
168. Zoski CG (2003) J Phys Chem B 107:6401
169. Fernandez JL, Walsh DA, Bard AJ (2005) J Am Chem Soc 127:357
170. Fernandez JL, Mano N, Heller A, Bard AJ (2004) Angew Chem Int Ed Engl 43:6355
171. Fernandez JL, Bard AJ (2003) Anal Chem 75:2967
172. Liu B, Bard AJ (2002) J Phys Chem B 106:12801
173. Sklyar O, Wittstock G (2002) J Phys Chem B 106:7499
174. Sklyar O, Treutler TH, Vlachopoulos N, Wittstock G (2005) Surf Sci 597:181
175. Treutler TH, Wittstock G (2003) Electrochim Acta 48:2923